Journal of Molecular Structure 1244 (2021) 130962

Contents lists available at ScienceDirect

Journal of Molecular Structure

journal homepage: www.elsevier.com/locate/molstr

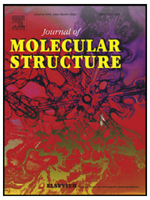

Spectroscopic characterization and binding interaction of heavy metal onto the surface receptor of the azobenzene: DFT and experimental approach

Marwa Chaabene[a,*], Soumaya Agren[b], Jamal El Haskouri[c], Abdul-Rahman Allouche[d], Lahcini Mohamed[e,f], Rafik Ben Chaâbane[a], Mohamed Hassen V Baouab[b]

[a] *Laboratory of Advanced Materials and Interfaces (LIMA), Faculty of Sciences of Monastir, University of Monastir, Avenue of the Environment, 5000 Monastir, Tunisia*
[b] *Research Unit Materials and Organic Synthesis (UR17ES31), Preparatory Institute for Engineering Studies of Monastir, University of Monastir, Avenue of the Environment, 5000 Monastir, Tunisia*
[c] *Instituto de Ciencias de Los Materiales de la Universitad de Valencia, Calle Catedratico José Beltran 2, 46980 Paterna, Valencia, Spain*
[d] *Institute of Light and Matter, UMR5306 University of Lyon 1-CNRS, University of Lyon, 69622 Villeurbanne cedex, France*
[e] *Laboratory of Organometallic and Macromolecular Chemistry-Composites Materials, Faculty of Sciences and Technologies, Cadi Ayyad University, Avenue Abdelkrim Elkhattabi, B.P. 549, 40000 Marrakech, Morocco*
[f] *Mohammed VI Polytechnic University, Lot 660, Hay Moulay Rachid, 43150 Ben Guerir, Morocco*

ARTICLE INFO

Article history:
Received 1 March 2021
Revised 6 June 2021
Accepted 21 June 2021
Available online 23 June 2021

Keywords:
Azobenzene
MEP
NPA
FMOs
Solvent effects and adsorption energy

ABSTRACT

The azobenzene 1-arylazo-2-naphthol has been synthesized and characterized by elemental analysis, ^{1}H NMR, IR and UV–Vis spectroscopies using both experimental and theoretical methods. The MEP, NPA and FMOs have also been performed at the DFT/B3LYP-D3 level with different solvents in order to investigate the solvent's effect. The energetic behavior of the compound has been examined in the gas phase and in solvent media using the integral equation formalism polarizable continuum model (IEF-PCM). Solvents had sligth significant effect on NPA values whereas both molecules hardness and stability decrease along with increasing of the solvent's polarity. Vibrational and absorption analysis showed no significant azo±hydrazone tautomerism. Theorically, the title molecule calculated in Acetonitrile solvent is the most reactive. The observed red shifts are explained by the large extension of the π conjugated system and the blue shifts confirm the appearance of several tautomeric forms of the studied azo-benzene which lead to a marked improvement in photochemical stability. The cation binding properties of azo benzene as absorption sensor for Cu^{2+}, Mg^{2+}, Ni^{2+} and Zn^{2+} cations were reported. The highest adsorption energy in both gas and liquid phase corresponds to the complexes Azoic/Ni^{2+} then in Azoic/Cu^{2+} and somewhat in Azoic/Zn^{2+}complex. The lowest adsorption energy is given to Azoic/Mg^{2+} complex. After cations chemisorption on azoic molecule a bathochromic shift is observed in the optical spectra, particularly for Azoic/Ni^{2+} complex, which is the proof of interaction between azoic compound and mentioned cations. The electronic proprieties and the vibrational spectra can therefore be used to detect the presence of different cations and the azobenzene shows appropriate properties to constitute good cations (Ni^{2+} and Cu^{2+}) sensors.

1. Introduction

With the expansion of the modern industry, agriculture and transport, heavy metal pollution has become a serious problem and an important factor in environmental pollution. Heavy metal contamination is a widespread contamination with a long-term effect and it is hard to eliminate because of its persisting nature. The cycling of organic materials and the exchange of energy, resulting in the transmission and enrichment of heavy metals through food chains, which ultimately endangers human health [1]. Recent investigations have found labile zinc to be severely involved in the human pathophysiology and neurology. For particular, failure in zinc homeostasis is implicated in the progression of prostate cancer as well as Alzheimer's disease [2,3]. Cu^{2+} is known to have a toxic effect on cells due to cellular apoptosis due to Cu^{2+} induced hydroxyl radicals [4]. It has also been documented that a

---

[*] Corresponding author.
E-mail address: marwachaaben0@gmail.com (M. Chaabene).

https://doi.org/10.1016/j.molstruc.2021.130962

significantly elevated level of Cu^{2+} is damaging to various organs, comprising the liver, kidneys, and brain [5] which leads to organ disfunction and neuro-degenerative diseases. Mercury, can cause to organisms and environment even at low concentrations [6,7]. When cobalt achieves a certain level in the human body, it causes and stimulates vasodilation, flushing and cardiomyopathy, blood and kidney adverse effects and other respiratory and central nervous system disorders. Simultaneously, animals deprived of cobalt show growth retardation, anemia, a loss of appetite and decreased lactation [8]. In addition, Nickel compounds are believed to cause cancer [9]. Some new investigations have shown that Pb^{2+} can enter the human body from wastewater and waste residues and cause damage to the haematopoiesis, nervous system and kidneys, resulting in chronic poisoning [10–12]. A lack of Magnesium can damage more than 300 enzyme systems that regulate various biochemical reactions in the body. These reactions involve proteins synthesis, muscle and nerve activity [13]. The Detection of chemical species is of major concern in a variety of fields, comprising environmental, medical and biological domains, and security. It is well recognized that recently, the increasing pressure from environmental authorities has led to the establishment of release standards, which in turn necessitate the effective use of chemical remediation and purification processes [14]. The design as well as the development of novel sensitive and specific chemosensors for the environmentally and biologically important heavy and transition metal ions have been strongly focused on over last few years [15–20]. These conventional approaches suffer greatly from the expensive cost of the instruments, complicated sample pre-treatment processes and rigorous experimental requirements [21]. On the other hand, it is required to transmit selectivity to the ion sensor for a material that has a great affinity for a certain metal ion but has a low sensitivity to other metals. In deed, the synthesis of azobenzene was shown to be easy and fast [22]. Azo compounds have attracted much attention thanks to their versatile properties and their photosensitivity [23] as well as their ability of bonding through $N = N$ groups [24] which make them favorable for use in fiber dyeing [25], analytical chemistry and in biological reactions, in particular, sensing and recognition of cations, anions and biomolecules [23]. Furthermore, metals and their ions especially toxic metals such as Cu^{2+}, Mg^{2+},Ni^{2+}, etc. play an important role in several biological, environmental processes and they are quite significant in human health [23,26,27]. In addition, the determination of cations in a real sample is quite important with simpler, cheaper and faster methods than conventional techniques. Until now, the determination of cations can be attained by several analytical methods using spectroscopic techniques. Though, simpler methods for practical applications of the detection of any analyte of interest are wanted. Fluorimetric and colorimetric chemosensors can be alternative techniques instead of the traditional analytical methods for the determination of cations in real sample. Consequently, the development of chromogenic chemosensors for cations recognition has become an attractive research field and the synthesis of new additional chemosensor is still required.

In this paper, we focus on the synthetical, structural, vibrational and optical analysis of azobezene for the first time using both experimental and theoretical methods in different solvents (Acetonitrile, Chloroform, Cyclohexane, Dichloromethane, Ethanol, THF, Toluene and gas phase). The solvation treatment was selected as follows : The solvent's choice was done according to their proticity and polarity as well as its predictible effect on the tautomeric forms of the studied compound. In deed, we used cyclohexan, toluen and chloroform as non-polar aprotic solvents. THF was chosen as a polar aprotic solvent and ethanol was employed for its obvious polarity and proticity. The concentration of the prepared samples is maintained to be 10^{-5} M. Moreover, we report the characterization and cation binding properties of azobenzene as an adsorption sensor for Cu^{2+} [28], Mg^{2+} [29], Ni^{2+} [30] and Zn^{2+} [31,32] cations. Furthermore, the coordination and the structural features of the cations complexes of azobenzene have been demonstrated by computational calculations at DFT and TD-DFT levels, where the presence of a number of heteroatoms (-N,-O) in azoic molecule makes it suitable for the recognition of different cations [33].

2. Experimental section

2.1. Materials and methods

^{1}H NMR spectra were measured on Bruker 300 MHz NMR spectrometer. FTIR spectrum was measured on a Perkin Elmer spectrum two ranging from 350 to 8300 cm^{-1} with DTGS as a detector. UV–vis absorption spectra were obtained on a SPECORD PLUS ranging from 190 to 1100 nm.

2.2. Quantum chemical calculation

Chemical calculations were performed by means of the Gaussian09 D.01 package [34] using the DFT method with the B3LYP functional, as it is the most suitable for reactivity studies. The results were analyzed using the graphical interfaces Gabedit [35] and gaussview software [36]. 6–311++G (d, p) base were used for the carbon (C), oxygen (O), hydrogen (H) and azote (N) atoms, while the def2tzvpp one was investigated for Ni^{2+}, Cu^{2+}, Mg^{2+} and Zn^{2+}. All the reported computations were performed using the dispersion-including B3LYP-D3 method to adequately describe the dispersion interactions between a particle and its neighbors in a given radius, via a simple pair-wise force field summed to the pure DFT energy [37]. The ^{1}H calculations used the Gauge-Independent Atomic Orbital (GIAO) [38] method. In all the cases ^{1}H for the test molecules were corrected with a chemical shift (δ/ppm) relative to simulated values for tetramethylsilane (TMS), computed at the same level. Calculations of vibrational IR frequencies of Azoic molecule before and after the adsorption of different cations have been carried out with the same method as geometry optimization in gas phase. It has been confirmed that these structures correspond to the characteristics of the local minimum by the absence of an imaginary mode. Natural population analysis (NPA) calculations and the theoretical electronic absorption spectra have been simulated by using B3LYP-D3 and CAM/B3LYP-D3 method respectively. NPA and the theoretical and experimental UV–vis absorption measurements were carried out at room temperature in seven kinds of solvent (Acetonitrile, Chloroform, Cyclohexane, Dichloromethane, Ethanol, THF and Toluene), also in the gas phase in order to evaluate the solvent effect to the atomic charge distribution over the chemical bonding, total energy, gap energy, HOMO and LUMO energies, chemical reactivity descriptors and dipole moment of the studied azo-benzene compound. The computations were done with 6–311++G (d, p) basis set using the polarizable continuum model (PCM) [39].

In addition, the adsorption energy in the gas phase ($\mathbf{E_{ad/gas}}$) calculated was based on the following expression:

$$\mathrm{Ead/gas} = \mathrm{EComplex} \; -- \; (\mathrm{EAzoic} + \mathrm{ECations}) + \mathrm{EBSSE} \qquad (1)$$

Where $E_{complex}$ is the total energy of cations adsorbed on Azoic molecule. E_{Azoic} is the total energy of isolated Azoic molecule, and $E_{cations}$ is the total energy of isolated cations Ni^{2+}, Cu^{2+}, Mg^{2+} and Zn^{2+}. The counterpoise method is used to correct the basis superposition error (E_{BSSE}) [40]. We have also calculated the solvation energy ($E_{ads/solv}$), using a Hess cycle, as the optique detection of all cations by the azoic molecule is investigated in an aqueous

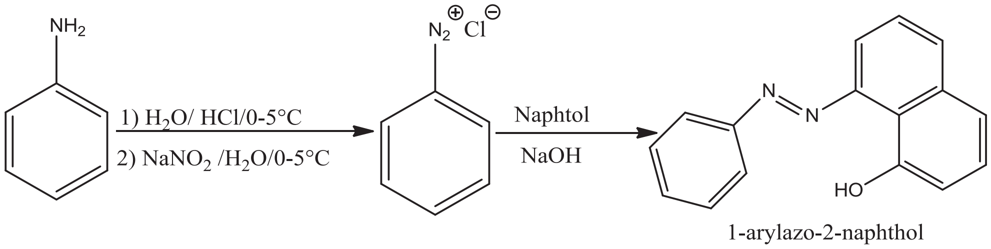

Scheme 1. General scheme for the synthesis of Azoic molecule.

medium. $E_{ads/solv}$ is calculated from Eq. (2) [41]

$$\mathbf{Ead/solv} = \mathbf{Eads/gas} + \mathbf{Esolv}\ (\mathbf{Azoic} + \mathbf{cations}) - \mathbf{Esolv}\ (\mathbf{cations}) - \mathbf{Esolv}\ (\mathbf{Azoic}) \quad (2)$$

Where $E_{ads/gas}$ is the adsorption energy in gas, E_{solv} (azoic), E_{solv} (cations) and E_{solv} (Azoic+cation) are the solvation energies of azoic molecule, cations, and complexes, respectively. Negative energy adsorption indicates a favorable interaction (the most stable structure relates to the largest negative value of energy), whereas positive energy adsorption indicates an unstable system [42].

The NPA analysis were performed again to investigate the direction of the charge transfer between our synthesized compound (Azoic) and the different cations in the complexe.

The UV–vis spectra of isolated Azoic molecule and Azoic/cations complexe are calculated at TD-DFT/CAM-B3LYP-D3/6–311++ *G* (d, p) level of theory [43].

Furthermore, by using the frontier molecular orbitals (Highest Occupied Molecular Orbital (HOMO) and Lowest Unoccupied Molecular Orbital (LUMO)) different global reactivity parameters have been determined such as electronic gap energy (Eg), chemical potential (μ), global hardness (η) and global softness (σ) mentioned in [44]:

$$\boldsymbol{Eg} \approx \boldsymbol{E_{LUMO}} - \boldsymbol{E_{HOMO}} \quad (3)$$

$$\boldsymbol{\mu} = -[\boldsymbol{E_{HOMO}} + \boldsymbol{E_{LUMO}}]/2 \quad (4)$$

$$\boldsymbol{\eta} = [\boldsymbol{E_{LUMO}} - \boldsymbol{E_{HOMO}}]/2 \quad (5)$$

$$\boldsymbol{\sigma} = 1/\boldsymbol{\eta} \quad (6)$$

The chemical potential (μ) characterizes the escaping tendency of electron from a stable system. The chemical hardness (η) measures the resistance of a molecule to charge transfer. The global softness (σ) is the capacitance of the molecule to acquire charge.

When we assess the sensitivity of the sensor, the shift of the HOMO-LUMO energy gap (Eg) is obtained as follows:

$$\Delta\mathbf{Eg} = [(\mathbf{Eg}2 - \mathbf{Eg}1)/\mathbf{Eg}1] * 100\ \% \quad (7)$$

Where Eg_1 and Eg_2 are the values of the Eg for the isolated Azoic molecule and after detection of different cations, respectively.

2.3. Synthesis and characterization

The investigated azo compound; 1-arylazo-2-naphthol has been obtained through the well-known diazotization process reported in literature (Scheme 1) [22]. This azoic dye is prepared as follows, 0.02 mol (1.9 g) of aniline has been dissolved in a mixture of Chlorohydric Acid (12 M) and distilled water (6 mL) at room temperature. The obtained solution was magnetically stirred and then cooled to 0–5 0C using a cold solution of an ice bath. A previously prepared 0.02 mol solution of sodium nitrite (1.37 g) in 8 mL of chilled water has been added drop by drop to the cold amine solution with constant stirring for 2 h by maintaining the reaction mixture 0–5 0C to achieve the diazotization reaction. This obtained diazonium salt solution was involved in the coupling reaction. A 0.02 mmol of the naphtol solution was prepared by dissolving 2.88 g in the 16 mL of aqueous NaOH and 100 mL of chilled water keeping the temperature at 0–5–0 C. Then the diazonium chloride solution was added dropwise into the nucleophilic compound within one hour of stirring condition. The orange color evolution of the reaction mixture is the primary indicator that our diazonium salt has turned into a diazo compound. The non-evolution of the shade of the azobenzene obtained and followed by CCM marks the reaction's end. The resultant product was filtered off, washed a number of times with chilled water and air dried for a night.

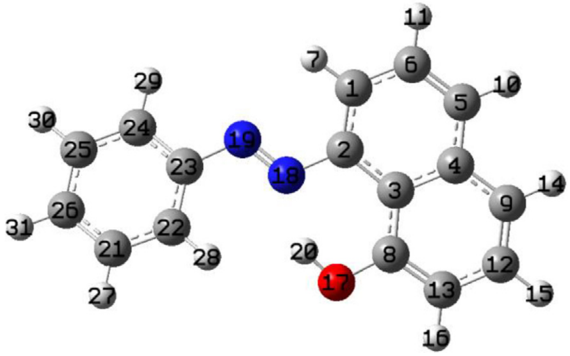

Fig. 1. Optimized structure of the Azoic molecule along with numbering of atoms.

3. Results and discussion

3.1. Molecular structure

The geometry parameters of 1-arylazo-2-naphthol were examined in different solvents using DFT calculation by B3LYP-D3 method with 6–311++ *G* (d, p) basis set in order to find the most stable geometry in the most suitable solvent. The choice of the solvent for this investigation was mainly based on the value of the calculated total energy. These values were calculated in different solvents (Acetonitrile, Chloroform, Cyclohexane, Dichloromethane, Ethanol, THF, Toluene and gas phase) using PCM approach and reported in Table 1. It is clearly observed that the highest value found with Acetonitrile to its efficiency.

In this part, all the calculations were made in Acetonitrile solvent, since the azoic is slightly the most stable in this solvent. The optimized structure of 1-arylazo-2-naphthol with the atomic numbering scheme is shown in Fig. 1.

Its correspondent energy and its dipole moment were found to be −801.870799 Hartree and 2.641 D, respectively. The calculated optimized geometrical parameters of the Azoic molecule in various

Table 1
The calculated electronic and quantum chemical parameters for the Azoic molecule in different solvents at DFT/B3LYP-D3/6–311++ *G* (d, p).

Solvents	Acetonitrile	Chloroform	Cyclohexane	Dichloromethane	Ethanol	THF	Toluene	Gas
E_T (a, u)	−801.870799	−801.868522	−801.865988	−801.86968	−801.870626	−801.869403	−801.866571	−801.863047
E_g (eV)	2.799	2.770	2.732	2.785	2.797	2.781	2.741	2.683
E_{HOMO} (eV)	−5.891	−5.829	−5.763	−5.860	−5.886	−5.852	−5.778	−5.700
E_{LUMO} (eV)	−3.092	−3.059	−3.031	−3.075	−3.090	−3.071	−3.037	−3.017
μ (eV)	4.492	4.444	4.397	4.468	4.488	4.462	4.408	4.359
η (eV)	1.400	1.385	1.366	1.393	1.398	1.391	1.371	1.342
σ (eV^{-1})	0.715	0.722	0.732	0.718	0.715	0.719	0.730	0.745
μ_D (D)	2.641	2.451	2.230	2.548	2.627	2.526	2.282	1.953

Table 2
Selected bond distances (Å) and bond angles (°) of the Azoic molecule calculated in various solvents by DFT method: compared with available theoretical and experimental results (first and second lines respectively), for similar compound.

Solvents	Acetonitrile	Chloroform	Cyclohexane	Dichloromethane	Ethanol	THF	Toluene	Gas	Litera.
Bond length (Å)									
O_{17}–H_{20}	0.988	0.987	0.986	0.988	0.988	0.987	0.986	0.985	0.68 [44]
C_8–O_{17}	1.359	1.357	1.355	1.358	1.359	1.358	1.356	1.353	1.34 [44]
C_3–C_8	1.434	1.434	1.435	1.434	1.434	1.434	1.434	1.435	1.39 [44]
C_2–C_3	1.437	1.437	1.437	1.437	1.437	1.437	1.437	1.437	1.402 [45] 1.417 [46]
C_2–N_{18}	1.413	1.413	1.413	1.413	1.413	1.413	1.413	1.413	1.397 [45] 1.394 [46]
N_{18}–N_{19}	1.276	1.276	1.276	1.276	1.276	1.276	1.275	1.275	1.261 [45] 1.276 [46]
N_{19}–C_{23}	1.416	1.416	1.416	1.416	1.416	1.416	1.416	1.416	1.414 [45] 1.415 [46]
C_{22}–C_{23}	1.406	1.406	1.406	1.406	1.406	1.406	1.406	1.405	1.406 [45] 1.396 [46]
C_{22}–H_{28}	1.082	1.082	1.082	1.082	1.082	1.082	1.082	1.082	–-
N_{18}-H_{20}	1.731	1.734	1.738	1.733	1.732	1.733	1.737	2.741	1.67 [44]
Bond angle (°)									
C_8-O_{17}-H_{20}	107.4	107.4	107.4	107.4	107.4	107.4	107.4	107.4	–-
C_3-C_8-O_{17}	122.3	122.4	122.6	122.3	122.3	122.3	122.4	122.5	123.1 [44]
C_2-C_3-C_8	124.3	124.4	124.4	124.4	124.4	124.4	124.4	124.4	–-
C_3-C_2-N_{18}	116.7	116.8	116.8	116.8	116.8	116.8	116.8	116.8	–-
C_2-N_{18}-N_{19}	117.3	117.3	117.3	117.3	117.3	117.3	117.3	117.3	116.2 [45] 113.3 [46]
N_{18}-N_{19}-C_{23}	115.9	115.9	115.9	115.9	115.9	115.9	115.9	115.9	114.6 [45] 113.5 [46]
N_{19}-C_{23}-C_{22}	125.7	125.8	125.8	125.7	125.7	125.7	125.8	125.9	124.7 [45] 125.2 [46]
C_{23}-C_{22}-H_{28}	120.2	120.1	120.1	120.2	120.2	120.2	120.1	120.1	–-

solvents are enumerated in Table 2 and compared with theoretical and experimental data available in literature for similar compound [45–47]. These optimized structures are helpful in computing a variety of parameters further. The optimized bond lengths of C_2–C_3, C_2–N_{18}, N_{19}–C_{23} and C_{22}–H_{28} are the same in different solvents with the value of 1.437, 1.413, 1.416 and 1.082 Å respectively. The bond angles of (C_8–O_{17}–H_{20}), (C_2–N_{18}–N_{19}) and (N_{18}–N_{19}–C_{23}) are not changed in the different solvents. Computed values of most of the bond lengths and bond angles have shown very close values in these solvents. Therefore, it can be noticed that the solvent has a very small effect on optimized geometrical parameters values. It is evident to mention that the majority of the experimental values of bond lengths and bond angles are slightly shorter than the theoretical ones. This discrepancy may be explained by the fact of hydrogen bonding interactions in the solid phase that are not taken into consideration in the calculations [48,49]. As shown in Table 2, most of the calculated values have shown good agreement with theoretical and experimental values available in literature.

Molecular electrostatic potential (MEP) mapping is very useful in the investigation of the molecular structure with its physiochemical property relationships [50,51]. It is obtained at the B3LYP-D3/6–311++*G* (d, p) optimized geometry. The negative (red) regions are related to electrophilic reactivity and the positive (blue) regions to nucleophilic reactivity sites as shown in Fig. 2. The color code maps for the Azoic compound were predicted in the range between −0.04 a.u and 0.04 a.u. The MEP is the best suitable tool for the identification of inter and intramolecular interaction sites [52]. Intramolecular O_{17}–$H_{20}\cdots N_{18}$ stabilizes the title molecule. The molecular electrostatic potential map indicates that the region around the oxygen atoms (O_{17}) linked with carbon through the double bond was the most negative potential region (red). Moreover, a negative electrostatic potential zone occurs on the imine

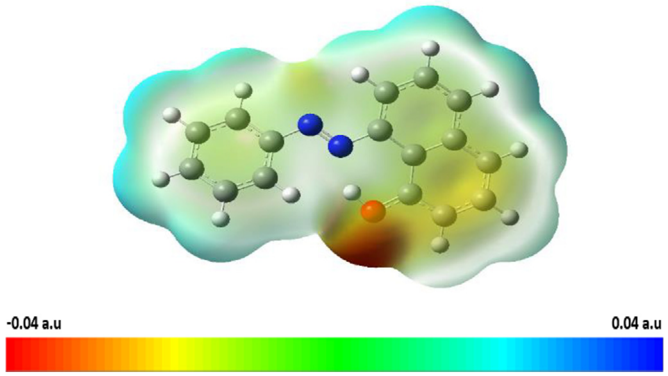

Fig. 2. The total electron density mapped with electrostatic potential of Azoic molecule in Acetonitrile solvent.

Table 3
Experimental and theoretical calculation NMR of ^{1}H for of the Azoic molecule.

Atom	δ_{exp}(ppm)	δ_{theo}(ppm)
$\mathbf{H_{7}}$	8.55	8.72
$\mathbf{H_{10}}$	8.53	8.55
$\mathbf{H_{11}}$	7.76	7.97
$\mathbf{H_{14}}$	7.76	7.80
$\mathbf{H_{15}}$	7.43	7.85
$\mathbf{H_{16}}$	6.90	7.53
$\mathbf{O_{17}H_{20}}$	15.70	15.81
$\mathbf{H_{27}}$	7.57	7.90
$\mathbf{H_{28}}$	7.96	8.15
$\mathbf{H_{29}}$	7.93	8.51
$\mathbf{H_{30}}$	7.55	8.09
$\mathbf{H_{31}}$	7.36	7.99

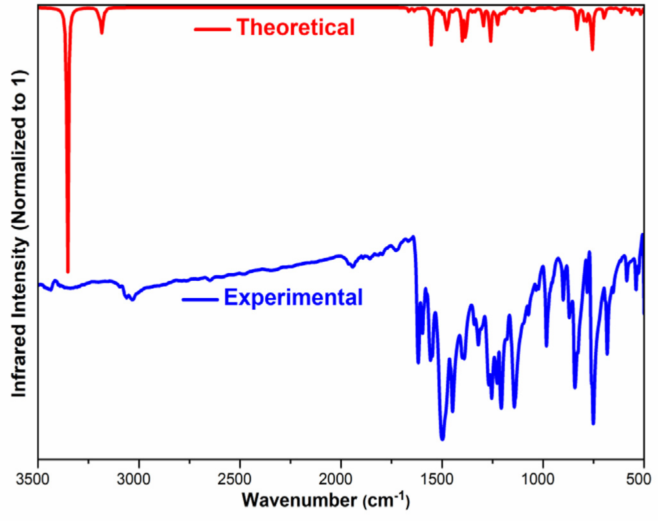

Fig. 3. Comparison of experimental and theoretical FT-IR spectra for the Azoic molecule.

N_{19} and N_{18}. Positive MEP results are on hydrogen atoms of the title molecule. Negative and positive electrostatic potential sites give information about the possible sites having hydrogen bondings. Therefore, Fig. 2 verifies intramolecular $O_{17}\_H_{20}\cdots N_{18}$ interactions.

3.2. NMR spectrum analysis

Multinuclear magnetic resonance spectroscopy is a very advantageous tool for the study of organic compounds stucture elucidation. The recorded and computed proton chemical shifts in DMSO solution with respect to TMS are gathered in Table 3. Theoretical chemical shifts were computed using DFT/GIAO methodology as well as 6–311++*G* (d, p). Experimental Chemical shifts were also reported in parts per million relative to TMS. The proton atom's positions were numbered as in Fig. 1. The analysis of magnetic properties of 1-arylazo-2-naphthol was identified by combined use of ^{1}H NMR spectroscopy and quantum chemical calculations. The theoretical ^{1}H chemical shifts have been compared with the recorded data. Azoic (a); $\delta = 15.7$ ppm (s, $J = 1.00$, $_{1}$H, OH), 6.9 ppm (d, $J = 1.804$, $_{2}$H), 7.43–8.55 ppm (td, dd, $J = 6.135$, $_{6}$H), 7.43–7.36–7.93 ppm (m, $J = 5.404$, 5H).

The hydroxyl proton exhibits a singlet resonance in the region of 15.7 ppm and 15.81 ppm for the experimental and theoretical spectra, respectively. The high hydroxyl band observed in this range is assigned to a strong intramolecular charge transfer interaction [53] involving the whole studied molecule. This trend is especially observed for azo groups [54]. The aromatic ring protons of the investigated compound were observed from 6.90 to 8.55 ppm for the experimental spectra and from 7.53 to 8.72 ppm for the theoretical data. The corresponding protons appear at lower field by comparison of those cited in literature [46] because of the strong electron delocalization of benzen rings. The resonance signals for H_{30} and H_{27} were hardly assigned. Mesomeric effect produces an electron excess which causes dishielding in the ortho position sush as H_{27} relatively-low resonance [55]. In the light of these results, we clearly notice that the calculated ^{1}H NMR chemical shifts for the title compound were in a satisfactory agreement with the experimental results. These findings indicate that the employed density functional method provides valuable informatuion for our title compound charecterization. This computational method was also employed in our recent studies [56] and shows that the predicting results values are coinciding very well with the observed frequencies.

3.3. Vibrational analysis

In the present study, we have performed a detailed frequency calculation using DFT computed by B3LYP/6–311++*G* in order to get the subject of the spectroscopic signature of the studied azoic dye: 1-arylazo-2-naphthol. The comparative experimental and theoretical FT-IR spectra are shown in Fig. 3. The experimentally-observed IR bands and the calculated frequencies as well as their assignments are summarized in Table 4. The scaled frequencies are also provided in Table 4 along with unscaled frequencies [57] where the theoretical harmonic frequencies were scaled down uniformly by a factor of 0.987 (for wave numbers under 1800 cm^{-1}) and 0.961 (for those over 1800 cm^{-1}) for B3LYP-D3/6–311++*G*(d, p) level of theory, which accounts for systematic errors caused by basis set incompleteness, vibrational anharmonicity and neglect of electron correlation [58].

The assignments for the studied molecular system are essentially proposed on the basis of frequency agreement between simulated and experimental fundamentals. As a general overview, the experimental spectrum complements the simulated spectrum and both FT-IR spectra confirm the proposed structure.

The 1-arylazo-2-naphthol FT-IR spectra exhibited characteristic bands along with their appropriate shifts due to several bond's formation. The studied compound displayed the typical C–H as well as the skeletal vibrations $C = C$ stretching and bending vibrations. The benzen ring modes involve C–C bonds and the vibrational frequencies are related to stretching modes of vibration of phenyl ring. The C–C stretching vibrations are estimated in the range from 800 to 1700 cm^{-1} [46]. These frequencies are not significantly influenced by the nature of the substituents [59] and are very much important and highly characterized by the aromatic ring itself [60]. These corresponding values agree with the literature data published for comparable azo dyes structures [61]. The C–H in-plane bending vibration generally occurs in the range of 1050 to 1520 cm^{-1} [46], while the C–H out of plane bending vibrations for substituted benzenes are in the region 500–1000 cm^{-1} [62]. Generally, the C–H out-of-plane bending with the highest frequencies have a weaker intensity than those absorbing at lower frequencies [62].

In the present work, the absorption peaks in the experimental FT-IR spectrum observed in the range of 1034–1668 cm^{-1} were ascertained to the C–H in plane bending vibrations. This theoretical C–H in plane bending vibrations were also observed in the same range from 1041 to 1644 cm^{-1}. Similarly, The FT-IR peaks occurring at 526, 540, 584, 653, 683, 752, 782, 841 and 984 cm^{-1} are assigned to the C–H out of plane bending vibrations and showed a good concurrence with theoretical observed frequencies at 511, 552, 572, 644, 691, 746,773, 821 and 981 cm^{-1} respectively. We

Table 4
B3LYP-D3/6–311++*G* (d, p) calculated vibrational frequencies (cm^{-1}) in gas phase.

ν_{calc} Unscaled	ν_{calc} ^{a} Scaled	ν $_{Exp}$	Vibration*
518	511	526	CH oopb + CC ipb+ CN ipb+ *C*–O-H twisting
559	552	540	CH oopb + CC ipb+ CN ipb+ *C*–OH str
580	572	584	CH oopb+ CC str+ CC ipb+ CN ipb +*C*–OH str
652	644	653	CH oopb + CC oopb+CN oopb+*C*–OH out of plane deformation
700	691	683	CH oopb + CC oopb +CN oopb
756	746	752	CH oopb+ OH oopb+ CC oopb
783	773	782	CH +oopb+CN oopb+ CC oopb
832	821	841	CH oopb + CN oopb+ *C*–O-H twisting
994	981	984	CH oopb
1055	1041	1034	CH ipb+ CC str+ CO str+ OH ipb
1108	1094	1073	CH ipb+ CC str+ OH ipb
1189	1174	1142	CH ipb+ CC str+ OH ipb
1206	1190	1207	CH ipb+ CC str+ CN str
1226	1210	1228	CC str+ CH ipb+ CN str+ CO str
1260	1244	1255	CC str+ CH *r*+ CO str+ CN str
1296	1279	1269	CH *r*+ CC str+ CO str+ OH *b*+ CN ipb+ NN str+ CN str
1352	1334	1341	CH ipb+ CC str+ NN str + CN b
1388	1370	1389	CC str+ CH ipb+ CO str+ CN ipb+ NN str+ CN str
1400	1382	1400	CC str+ CO str+ OH ipb+ CH ipb+ CN ipb+ NN str+ CN str
1473	1453	1448	CC str+ CH ipb+ CO str+ OH ipb+ NN str+ CN str
1480	1460	1500	CC str+ NN str+ CN str+ CO str+ CH *r*+ OH ipb
1553	1533	1558	CC str+ CH ipb+ CO str+ OH ipb+ NN str
1639	1618	1638	CC str+ NN str+ CH ipb+ OH ipb+ CN ipb
1666	1644	1668	CC str+ OH ipb+ CO *b*+ CH ipb+ NN str
3176–3217	3052–3092	3035–3331	CH str
3354	3223	3431	OH str

str: stretching; r: rocking; b: bending; oopb: out of plane bending; oop: out of plane; ipb: in plane bending.

* The majority of harmonic modes were composed of a variety of local modes. Only the local modes that have the most important contribution were listed in the Table.

can notice from Table 4 that the theoretical frequencies will match well with the experimental ones, after scaling.

The C–H out of plane bending vibrations are apparently not pure and contain important contributions of other modes sush out of plane C–N bending vibration [61]. Additionally, the assignment of C–N stretching frequency is a tough task since a large number of coupling interactions between rings of C–N stretching vibrations take place in this region [63]. C–N stretching absorption is usually observed in the region of 1200–1520 cm^{-1}for azoic dyes [13,11] and C–N bending vibrations appear in the range of 600–1510 cm^{-1} for example, the bands observed at 1207–1500 cm^{-1} in FT-IR are assigned as C–N stretching vibrations. The theoretically calculated wavenumbers at 1190–1460 cm^{-1} are assigned to C–N stretching vibrations. We noted also that the C–N bending vibrations gives rise to several characteristic bands at 526–841 cm^{-1} and at 1341–1638 cm^{-1} covering the spectral range. The bands were confirmed by their corresponding theoretical values appearing at 511–821 cm^{-1} and at 1334–1618 cm^{-1}.

The $N = N$ stretching vibrations are expected in the range from 1490 to 1525 cm^{-1}. This band is not significantly influenced by the substituents and the environment's nature [61]. In our case, the experimental $N = N$ stretching vibration appeared in the range of 1269–1668 cm^{-1} and shows a good harmony with the theoretical calculated values and similar published structures [61]. The hydroxyl group gave rise to three vibrations specifically stretching, in-plane and out-of plane bending vibrations.

The OH group vibration, one of the most sensitive bonds to the environment modification, shows obvious shifts in the hydrogen bonded species' spectra. The hydroxyl stretching vibrations are observed in the region around 3500 cm^{-1} [61-66]. The comparison of this band with the theoretical value shows a good harmony to the experimental data prediction that there is a descrepancy, that may be due to the fact that there is a strong intramolecular hydrogen bonding. The usual intra-molecular hydrogen bonding present in a six-membered ring would reduce the OH stretching band to 3559–3200 cm^{-1} region [67]. In the case of an unsubstituted phenol, the peak observed at 3657 cm^{-1} has been assigned to an hydroxyl stretching vibration in the gas phase [66]. Based on these facts, the medium band observed at 3431 cm^{-1} in the experimental spectrum is assigned to O-H stretching vibration. A comparison of this band with the theoretical value at 3223cm^{-1} shows an evident deviation of ~200 cm^{-1}. The difference between the computed and the experimental value may be essentially due to the presence of strong intramolecular hydrogen bonding [64]. The O-H in-plane bending vibration in phenolic compounds lies in the region 1150-1270 cm^{-1} [61] and is not affected due to OH hydrogen bonding unlike the stretching and out-of-plane bending frequencies [68]. In our case, the bands observed between 1034 and 1142 cm^{-1} and at 1400–1668 cm^{-1} are attributed to O-H in-plane bending vibration. The theoretically computed value at 1041–1174 cm^{-1} and at 1382–1644 cm^{-1} shows good agreement with our experimental observation. The O-H out-of-plane bending vibration for similar structures is around 290-320 cm^{-1} for non hydrogen bonded O-H and at 517-710 cm^{-1} for associated O-H [69]. In both inter-molecular and intra-molecular hydrogen bonds, the frequency is at a higher value than free O-H. In the same line of thought, the wavenumber increases with hydrogen bond strength because of the large amount of the required energy to the O-H bond twisting [70].

In the present study, the theoretical wavenumber of O-H in-plane bending vibration which were recorded between 1279 and 1644 cm^{-1} shows an excellent agreement with the experimental wavenumber at 1269 and 1644 cm^{-1} respectively. As a general trend, all OH vibration's modes appeared in the characteristic range and they are well approved. The observed bands in both experimental and theoretical spectra in the region of 1200–1700 cm^{-1} confirm the presence of C–OH in plane bending vibrations. These bands cover a wider range due to the extent of π conjuguation and charge delocalization [53,56]. The O–H strtching vibration occurs generally in region 3700–3550 cm^{-1} [71]. The presence of a stronger intra-molecular hydrogen shifts the O–H stretching

Table 5
NPA Charges of the important atoms of the Azoic molecule in different solvents.

Atom	H_{20}	O_{17}	C_8	C_3	C_2	C_1	H_7	N_{18}	N_{19}	C_{23}	C_{22}	H_{28}
Acetonitrile	0.489	−0.716	0.303	0.014	0.084	−0.178	0.232	−0.261	−0.182	0.087	−0.198	0.222
Chloroform	0.488	−0.710	0.306	0.015	0.085	−0.178	0.231	−0.261	−0.181	0.089	−0.196	0.221
Cyclohexane	0.486	−0.703	0.309	0.017	0.085	−0.177	0.230	−0.260	−0.180	0.091	−0.195	0.220
Dichloromethane	0.488	−0.713	0.305	0.015	0.084	−0.178	0.231	−0.261	−0.181	0.088	−0.197	0.221
Ethanol	0.489	−0.715	0.304	0.014	0.084	−0.178	0.232	−0.261	−0.182	0.087	−0.197	0.222
THF	0.488	−0.712	0.305	0.015	0.084	−0.178	0.231	−0.261	−0.181	0.088	−0.197	0.222
Toluene	0.487	−0.705	0.308	0.017	0.085	−0.177	0.230	−0.260	−0.181	0.090	−0.195	0.220
Gas	0.485	−0.695	0.312	0.018	0.086	−0.176	0.228	−0.259	−0.180	0.093	−0.193	0.219

bond to 3550–2000 cm^{-1} region [70]. In the present study, the wavenumbers observed at 3441 cm^{-1} and 3223 cm^{-1} in the experimental FT-IR spectrum and theoretical simulated spectrum. 200 cm^{-1} deviation from experimental to theoretical values is due to the presence of remarkable unharmonicity in this vibration as well as the O–H may have participated in a strong intermolecular hydrogen bonding in the title compound [72].

The harmonic frequencies by DFT calculations are usually higher than the corresponding experimental ones. This discrepancies between the experimental and the computed values may be caused by several factors. The environment is the first cause while the second factor seems to be the electron correlation approximate treatment, anharmonicity effects (where the experimental vibrational value is an unharmonic frequency whereas the calculated vibrational value is a harmonic frequency) and basis set deficiencies, etc. [73]. Furthermore, the interactions between the molecules make the frequencies shift to the lower frequencies.

[a] Obtained from the wave numbers calculated at B3LYP-D3/6–311++*G* (d, p) using scaling factors 0.987 (for wave numbers under 1800 cm^{-1}) and 0.961 (for those over 1800 cm^{-1}).

3.4. Natural population analysis

The atomic charges of the Azoic molecule were calculated by natural population analysis (NPA) using B3LYP-D3/6–311++*G* (d, p) level of basis set. It is used to understand the atomic charge distribution over the chemical bonding. The variation of bond length between atoms depends on the allocation of charges. The atomic charges on every atoms in the molecule gives an effective information about the electronic structure, acidic-basic nature and molecular polarizability [74]. The NPA analysis of the title compound were performed in different solvent using PCM model and gathered in Table 5. The plot of natural atomic charges for Azoic molecule is shown in Fig. 4(a). The O_{17} (−0.716; −0.695) atom has more negative charge than other atoms due to the formation of O–H…N hydrogen bonding. The carbon atoms attached to the nitrogen and oxygen atoms C_2, C_3, C_8 and C_{23} are positive thanks to the electron with drawing nature of electronegative atoms, other carbon atoms presented in the phenyl ring and naphthalene shows negative charges. The N_{19} atom shows (−0.182; −0.180) less negative charge compared with N_{18} (−0.261; −0.259) confirmed the formation of C–H…N hydrogen bonding. All hydrogen atoms show positive charge in which, H_{20} (0.489; −0.485) is more positive because of the electron with drawing nature of oxygen atom in the hydroxyl group. As shown in Table 5, we can notice that the solvent has a very small effect on NPA values. Indeed, the maximum shift between charges calculated with solvent and those obtained in gas phase is about 0.021 a.u observed for O_{17}.

For this reason, we chose to put the NPA analysis in Acetonitrile solvent.

3.5. Photophysical properties

3.5.1. Absorption properties

Ultraviolet and visible light absorption spectroscopy is a measure of a beam's reduction after it has passed through a studied sample or reflected from a sample surface [75,76]. To explore the solvent's impact on the absorption spectra and the photophysical properties of the synthesized azo dye: I-phenyl azo-2-naphthol, we have recorded its electronic absorption spectra (Fig. 5(a)) over the wavelength range 210–485 nm in six different solvents; Acetonitrile, Ethanol, THF, Toluene and cyclohexane. The spectroscopic analyses of the studied molecule are investigated by not only experimental means (at 10^{-6} M concentration and at room temperature) but also theoretically in the above-mentioned media and in Dichloromethane solvent. The theoretical calculations of the absorption spectra were done by TD-DFT method at CAM-B3LYP-D3/6–311++*G* (d, p) level of basis set in gas and other solvents which are represented in Fig. 5(b) in comparison with the experimental one. The calculated and experimental wavelengths from absorption peak, oscillator strength and (%) contribution from each transition of the studied azobenzene in various solvents are presented in Table 6.

The orange shade of the investigated dye wasn't influenced by the solvent nature which makes it suitable for industrial application [77]. The 1-arylazo-2-naphthol dyes can show significant azo±hydrazone tautomerism [77]. Thus, their visible absorption spectra sometimes show two absorption bands attributable to the two tautomers, and the ratio of the tautomers at equilibrium depends both on substituents in the dye and the nature of the solvent. Two factors are responsible for the tautomeric shift, i) selective solvatation depending on the two and three dimensional structures of the solvent [78], ii) the ability of the solvent to form strong intermolecular hydrogen bonds with particular tautomeric form.

As a general overview, the 1-arylazo-2-naphthol spectra exhibited similar and narrow absorption bands as well as comparable band intensities in all the solvents except for Acetonitrile solvent. As shown in Table 4, the experimental maximal wavelengths coincident reasonably with the calculated results. It is clear that there is no correlation between the polarity and proticity of the used solvents with the main absorption wavelength except for the Acetonitrile. Thanks to the hydroxyl substantial strength of the intra and intermolecular hydrogen bondings, electron delocalization and solvent interactions are limited which is confirmed from the theoretical calculations [45]. A relatively remarkable red shift for some bands and an increasing in the band's intensity is observed in cyclohexane spectrum (then in Toluene solvent) while a blue shift and a deacreasing in the band's intensity is observed in Acetonitrile spectrum and theoretical findings can support this viewpoint. According to several studies, the red shift is associated with the large extension of the π conjugated system [53,56,79,80]. Thus, the blue shift may indicate the appearance of several tautomeric forms of 1-arylazo-2-naphthol and the disappearence of the hydroxyl

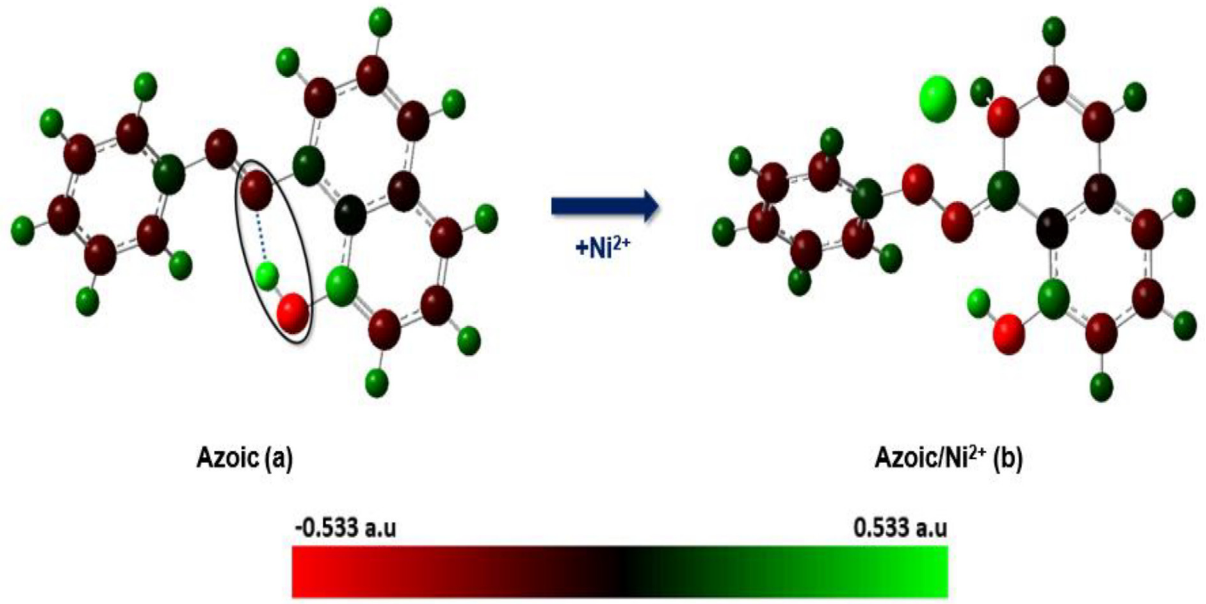

Fig. 4. NPA distribution of Azoic compound before (a) and after Ni capture (b) calculated at B3LYP-D3/6–311++G (d, p) level of theory in Acetonitrile solvent.

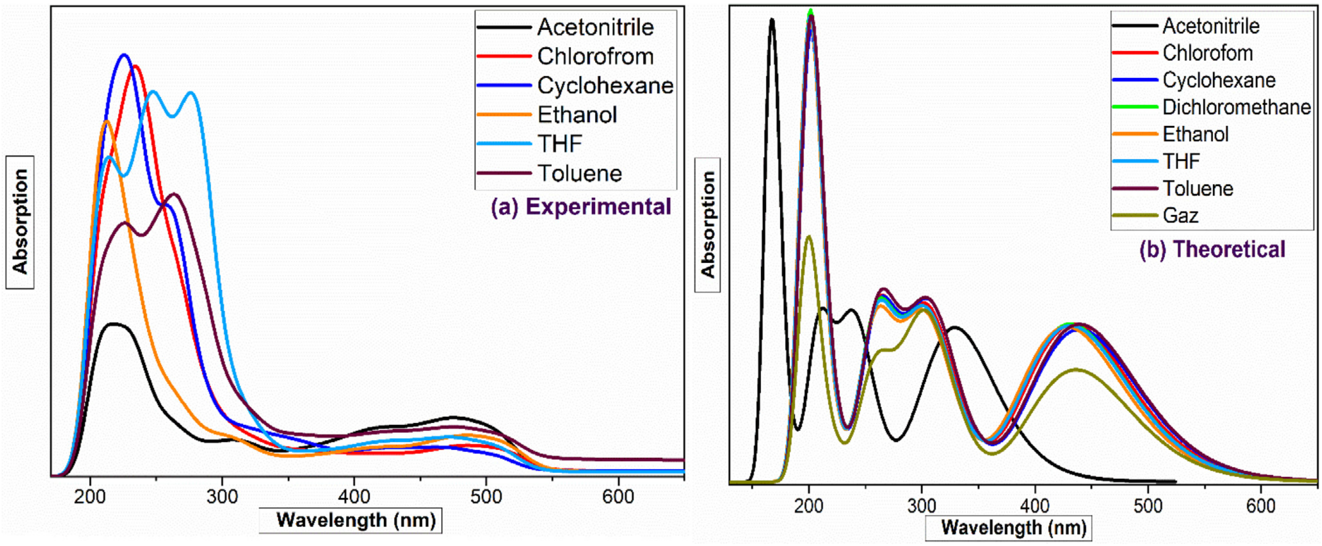

Fig. 5. The solvent effect on UV–Vis spectra of the title compound in Acetonitrile, Chloroform, Cyclohexane, Dichloromethane, Ethanol, THF, Toluene and gas phase.

donor group at certain wavelengths. It is well recognized that the intramolecular binding of hydrogen in a 1-arylazo-2-naphthol will frequently lead to a marked improvement in photochemical stability [81].

The ortho–hydroxyl substituted azo-azomethine compounds are distinguished by the possibility to be inferred from, selective solvation, the ability of the solvent to form stronger intermolecular H-bonds with a particular tautomeric form along with the intramolecular hydrogen bonding between C–N or $N = N$ and OH groups which generates several tautomeric forms as shown in Fig. 4(a). These diffrent tautomeric forms are generally instable [82]. Regarding the spectral properties of the studied molecule, we noticed that the maximal absorption bands emerged at the same optical range for all the solvents except for some bands for the spectrum record in Acetonitrile.

We also notice that the shorter wavelength UV band suffers a small shift on changing the solvent. Among studied solvent's effect, absorption maxima in Acetonitrile occur at lower wavelengths than in the less polar other solvents. The experimental absorption bands of the studied azobenzene recorded in acetonitrile showed five main characteristic absorption peaks at 210, 234, 268, 416 and 476 nm, respectively. These bands show good agreement with measured theoretical bands at 201, 258, 307, 417 and 452 nm, respectively. The peaks at 200 and 300 nm range are attributed to the n→ π^* transition of benzene and naphthalene ring, respectively. The peak located around 300 nm can be assigned to the n → π^* electronic transition of $N = N$ group [83]. The peaks in the range of 420 nm and the at 485 nm corresponds to the $\pi \rightarrow \pi^*$ transitions of the hydrazone form and azo, respectively [83,84]. The absorption peaks in all solvents exhibited smaller variations than in gas possibly due to the solvent effect.

In contrast, in the protic solvent ethanol obvious anomalies were observed, and the title dye with intramolecular hydrogen bonding, absorb at longer wavelengths in ethanol than in Acetoni-

Table 6
Calculated and experimental electronic transition parameters of the Azoic compound by a CAM-B3LYP-D3/6–311G++ method in different solvents.

Solvents	λ Exp (nm)	λ Cal (nm)	f (a.u)	Major and minor contributions (%)
Acetonitrile	210	201	0.313	H-1 →L + 2 (25%) H-2 →L + 1 (25%) H-3 →L + 1 (22%)
	234	258	0.250	H →L + 2 (50%) H-2 →L (30%) H →L + 1 (29%)
	277	307	0.230	H-1 →L (40%) H →L + 2 (21%) H-2 →L (36%)
	416	417	0.299	H →L (58%) H-1 →L (17%) H-3 →L (25%)
	476	452	0.157	H →L (58%)
Chloroform	217	202	0.460	H-2 →L + 1 (39%) H-1 →L + 1 (21%) H →L + 2 (13%)
	264	263	0.243	H →L + 1 (54%) H →L + 2 (28%) H-2 →L (25%)
	308	309	0.273	H-1 →L (43%) H →L + 2 (19%) H-2 →L (34%)
	421	423	0.283	H →L (57%) H-1 →L (18%) H-3 →L (30%)
	484	455	0.178	H →L (41%)
Cyclohexane	222	202	0.481	H-2 →L + 1 (44%) H →L + 2 (11%) H-1 →L + 1 (20%)
	259	264	0.254	H →L + 1 (52%) H →L + 2 (30%) H-2 →L (26%)
	318	311	0.283	H-1→L (43%) H-2 →L (36%) H →L + 1 (10%)
	424	428	0.257	H →L (56%) H-1 →L (18%) H-3 →L (34%)
	485	457	0.183	H →L (42%)
Dichloromethane	–-	202	0.412	H-2 →L + 1 (34%) H-1 →L + 1 (23%) H-3 →L + 1 (25%)
	–-	259	0.234	H →L + 2 (48%) H →L + 1 (34%) H-2 →L (28%)
	–-	308	0.260	H-1 →L (43%) H-2 →L + 1 (12%) H-2 →L (34%)
	–-	420	0.293	H →L (57%) H-3 →L (29%) H-1 →L (18%)
	–-	454	0.172	H →L (40%)
Ethanol	212	202	0.333	H-2 →L + 1 (27%) H-1 →L + 1 (25%) H →L + 2 (14%)
	259	258	0.248	H →L + 2 (50%) H →L + 1 (30%) H-2 →L (30%)
	305	307	0.236	H-1 →L (41%) H-2 →L (36%) H →L + 1 (10%)
	420	418	0.299	H →L (58%) H-3 →L (26%) H-1 →L (18%)
	483	452	0.160	H →L (40%)
THF	212	202	0.416	H-2 →L + 1 (34%) H-1 →L + 1 (23%) H →L + 2 (14%)
	247	259	0.236	H →L + 2 (48%) H →L + 1 (33%) H-2 →L (28%)
	280	308	0.256	H-2 →L (42%) H-2 →L (35%) H →L + 2 (20%)
	419	420	0.290	H →L (57%) H-3 →L (29%) H-2 →L (18%)
	482	454	0.169	H →L (40%)
Toluene	224	202	0.504	H-2 →L + 1 (44%) H-1 →L + 1 (19%) H →L + 2 (12%)
	263	264	0.278	H →L + 1 (51%) H →L + 2 (32%) H-2 →L (27%)
	304	310	0.298	H-1 →L (44%) H-2 →L (34%) H →L + 1 (10%)
	433	428	0.263	H →L (55%) H-3 →L (34%) H-1 →L (19%)
	485	457	0.193	H →L (42%)
Gas	–-	200	0.322	H-1 →L + 3 (34%) H-2 →L + 1 (26%) H-2 →L + 3 (10%)
	–-	258	0.217	H →L + 3 (44%) H-2 →L (32%) H →L + 3 (25%)
	–-	302	0.322	H-1 →L (52%) H-2 →L (29%) H-3 →L (26%)
	–-	429	0.218	H →L (60%) H-3 →L (28%) H-1 →L (17%)
	–-	455	0.100	H →L (40%)

trile. The deviation between experiment and theory may be resulted from solvent effects, where the solvent makes the molecule chemical environment simulation become very complex [46].

3.5.2. Frontier molecular orbital analysis

We have carried out calculations in seven different solvents (Acetonitrile, Chloroform, Cyclohexane, Dichloromethane, Ethanol, THF and Toluene) and in gas phase in order to evaluate the solvent's polarity effect on the energy gap, HOMO and LUMO energies, chemical reactivity descriptors and dipole moment of the studied Azoic dye. The computations were done by the CAM-B3LYP/6–311++*G* (d, p) level using IEF-PCM model and the results are given in Table 1. Hard molecules have a large HOMO–LUMO energy gap whereas soft molecules have a small HOMO–LUMO energy gap. As shown in Table 1, the small HOMO–LUMO energy gap corresponds to the title compound in gas phase (2.683 eV) then in Cyclohexane solvent (2.732 eV) which means small excitation energies. Therefore, hard molecules, with a large gap, correspond to the studied molecule in Acetonitrile solvent (2.799 eV), where their electron density changed more hardly than a soft molecule [56]. Electronic chemical potential is defined as the negative of electronegativity of a molecule [53]. The reactivity increases along with the increase of the chemical potential. Thus, the title molecule calculated in Acetonitrile solvent is more reactive than in other solvents. Global hardness is a useful concept to understand the behavior of chemical systems and is associated with the stability and reactivity of a chemical system [85]. The compound's hardness value is 1.400 eV in Acetonitrile. Accordingly, the molecule's hardness and stability decrease along with the increasing of the solvent's polarity in gas phase (1.342 eV) and in Cyclohexane solvent (1.366 eV). Global softness (σ) is a molecule's property that measures the extent of chemical reactivity [86]. Among the different solvents, 1-arylazo-2-naphthol have the greatest softness values in the gas phase than in Cyclohexane solvent while it has the weakest value of softness in the Acetonitrile solvent.

We can conclude from a close observation of Table 1 that the HOMO–LUMO energy gaps, the molecule's chemical potential and global hardness, have the highest values in acetonitrile and these values decrease along with the increasing of the solvent polarity (which are cyclohexane solvent and gas phase). The frontier molecular orbitals of azobenzene molecule before (Fig. 6(a)) and after Ni capture (Fig. 6(b)) in acetonitrile solvent were calculated with CAM-B3LYP-D3 method. Red and green colours represented the positive and negative phases of HOMO and LUMO respectively. It can be seen from this figure, that HOMO is localized mainly on the naphthalene ring and it slightly shifted to the π conjugated carbon atoms of the phenyl ring while the LUMO is mainly localized on the phenyl ring to which $N = N$- core is attached. The studied azoic molecule shows strong delo-calization of both HOMO and LUMO on the π-conjugation bridgecan. The qualitative picture

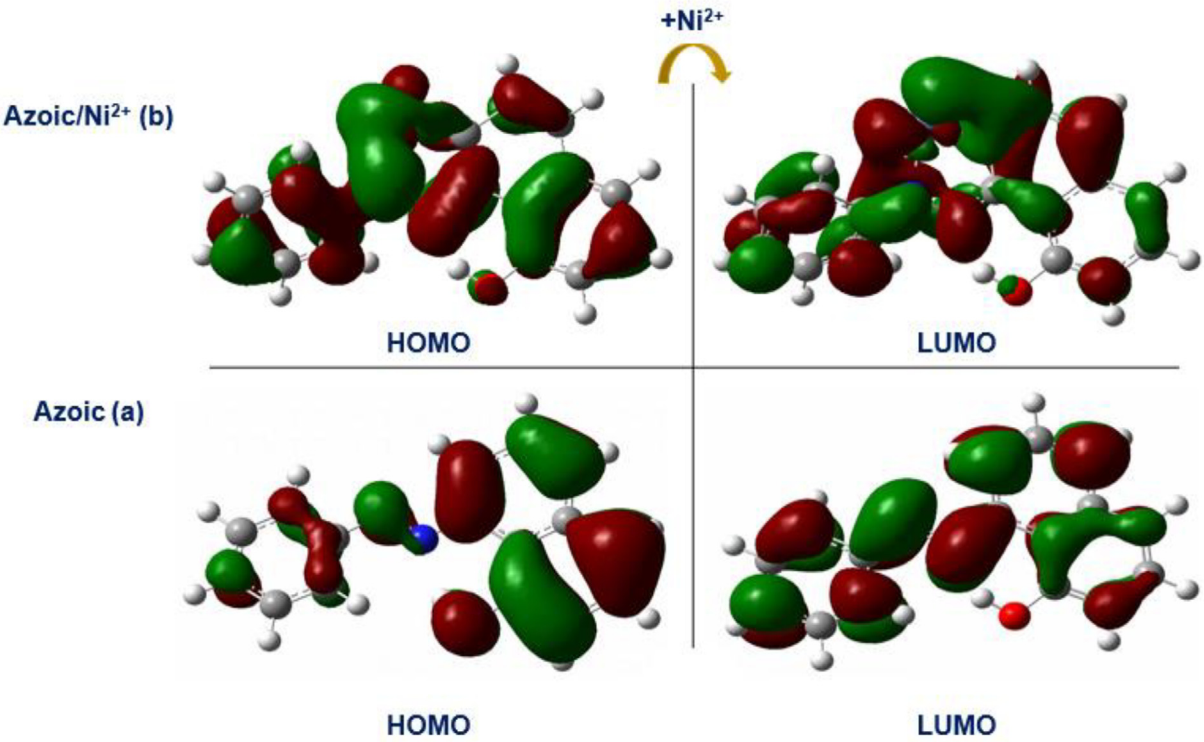

Fig. 6. Calculated frontier molecular orbitals of azobenzene molecule before **(a)** and after Ni capture **(b)** in acetonitrile solvent with CAM-B3LYP-D3 method.

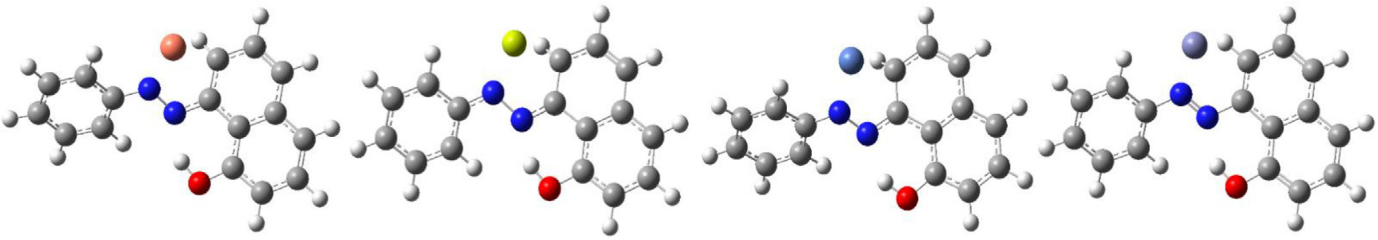

Atom	H_7	C_1	C_2	N_{18}	N_{19}	C_{23}	C_{24}	H_{29}	$Cation_{32}$
Isolated Azoic	0.232	-0.178	0.084	-0.261	-0.182	0.087	-0.173	0.224	----
Azoic/Ni^{2+}	0.293	-0.375	0.219	-0.214	-0.159	0.100	-0.138	0.238	1.126
Azoic/Cu^{2+}	0.126	-0.089	0.111	-0.133	-0.109	0.046	-0.061	0.111	0.463
Azoic/Mg^{2+}	0.234	-0.228	0.126	-0.206	-0.171	0.095	-0.128	0.217	1.017
Azoic/Zn^{2+}	0.241	-0.236	0.129	-0.179	-0.126	0.091	-0.127	0.225	1.075

(a) Azoic/Cu^{2+} (b) Azoic/Mg^{2+} (c) Azoic/Ni^{2+} (d) Azoic/Zn^{2+}

Fig. 7. The optimized structures of the complexes formed between Azoic compound and Cu^{2+} **(a)**, Mg^{2+} **(b)**, Ni^{2+} **(c)** and Zn^{2+} **(d)** cations.

proves a flow of electron density (intramolecular charge transfer) from the electron-donor group byway of the p-electron bridge to the electron acceptor group (except for the hydroxyl group) [46].

4. Cation binding studies

4.1. Structural, energetic and electronic analysis

The optimized structures of azoic complexes (Azoic/Cu^{2+} **(a)**, Azoic/Mg^{2+} **(b)**, Azoic/Ni^{2+} **(c)** and Azoic/Zn^{2+} **(d)**) are shown in Fig. 7, where only complexes with the largest adsorption energy will be discussed in this section. Structural and energetic parameters in both gas and liquid phases are gathered in Table 7.

As represented in the previous figure, we notice that the best adsorption mode of these different cations is located around the strong hydrogen bonding zone. In particular, they are closer to the nitrogen atom (N_{19}) with a N_{19}–Cu^{2+}, N_{19}–Mg^{2+}, N_{19}–Ni^{2+} and N_{19}-Zn^{2+} distances of 2.011, 2.093, 1.877 and 2.411 Å respectively in gas phase and of 1.996, 2.264, 1.857 and 2.211 respectively in Acetonitrile solvent. It's clear that the distances N_{19}-cations are smaller in the acetonitrile solvent than in the gas phase except for the distance N_{19}–Mg^{2+} which is greater in this phase.

Table 7
Distances of N_{19}-cations (in Å), adsorption energies (E_{ad}) for different complexes, HOMO, LUMO energies, gap energy (E_g), ΔE_g indicates the change of E_g after the cations adsorption and dipole moment in Debye of metal cations on Azoic molecule in both gas and liquid phases.

Azoic	$d_{ad,\ gas}$ (N_{19}-cations) (Å)	$d_{ad,\ solv}$ (N_{19}-cations) (Å)	$\Delta E_{ad,\ gas}$ (Kcal.mol^{-1})	$\Delta E_{ad,\ solv}$ (Kcal.mol^{-1})	$E_{HOMO,\ solv}$ (eV)	$E_{LUMO,\ solv}$ (eV)	Eg $_{solv}$ (eV)	ΔEg $_{solv}$	$\mu_{D,solv}$ (D)
Ni^{2+}	1.877	1.857	−330.374	−119.743	−7.140	−5.278	1.862	−33.476	10.118
Cu^{2+}	2.011	1.996	−309.335	−79.854	−7.424	−4.547	2.877	2.787	7.043
Mg^{2+}	2.093	2.264	−173.437	−8.979	−6.391	−3.980	2.411	−12.790	26.440
Zn^{2+}	2.411	2.211	−242.196	−18.900	−6.486	−4.172	2.314	−17.328	20.862

Table 8
Calculated charge by natural population analysis (Q_{NBO}) of some atoms of azoic complexes using B3LYP-D3/6–311++G (d, p).

Atom	H_7	C_1	C_2	N_{18}	N_{19}	C_{23}	C_{24}	H_{29}	$Cation_{32}$
Isolated Azoic	0.232	−0.178	0.084	−0.261	−0.182	0.087	−0.173	0.224	–-
Azoic/Ni^{2+}	0.293	−0.375	0.219	−0.214	−0.159	0.100	−0.138	0.238	1.126
Azoic/Cu^{2+}	0.126	−0.089	0.111	−0.133	−0.109	0.046	−0.061	0.111	0.463
Azoic/Mg^{2+}	0.234	−0.228	0.126	−0.206	−0.171	0.095	−0.128	0.217	1.017
Azoic/Zn^{2+}	0.241	−0.236	0.129	−0.179	−0.126	0.091	−0.127	0.225	1.075

According to MEP maps, this corresponds to an electrophilic attack of the different cations on N_{19} atom (nucleophilic region). Upon cations adsorption, atomic charge on N_{19} (see Table 8) decreases from about −0.182 in isolated azoic compound to −0.109 a.u. in azoic/Cu^{2+}while all cations get positively charged and the most positively charged cation is Ni^{2+} (1.126 a.u) (Fig. 4(b)). Thus, we can say that the adsorption process of cations occurs through metal coordination, i.e. σ bonding formation between N_{19}-cations moieties. This bond formation is made possible by an electron transfer from the cations (Cu^{2+}, Mg^{2+}, Ni^{2+} and Zn^{2+}) to the azoic compound. Here, we developed the azoic dye as chemosensor containing the hydroxyl and $N = N$- core as an electron acceptor group. While the naphthalene and the phenyl moiety act as a donor site. Consequently, all cations are close to the strong hydrogen-bonding zone through relatively clear chemisorption process. The planarity of the azoic molecule is deformed, for each Azoic/cations complex, where the presence of different cations specially the Ni^{2+} close to the donating azotes atoms of the azoic group of the studied compound tends to increase the charge density and the pre-organization of the benzen rings.

Data listed in Table 7 indicate that Azoic/cations complexations are exothermic, as all calculated adsorption energies are negative. For each, adsorption energies corrected for BSSE at the B3LYP-D3/6–311++G (d, p) level of theory were simulated. The values of adsorption energies indicate that the solvation effect is very important, especially the solvation energies of cations are important and decrease the interaction energy significantly from gas phase to the liquid one. Calculations show that the most stable complex, in both gas and liquid phase, is Azoic/Ni^{2+} where the adsorption energy is found to be −330.374 kcal/mol and −119.743 kcal/mol respectively. Azoic is consequently the most reactive compound with Ni^{2+} then Cu^{2+} respectively.

4.2. UV–Vis absorption spectra

The optical absorption spectra of Azoic/cations complexes are studied experimentally and theoretically by using TD-DFT/CAM-B3LYP-D3/6–311G++ (d, p) method. Fig. 8 shows spectra for azoic compound before and after cations adsorption in the acetonitrile solvent and their wavelengths are given in Table 9. One can notice that after the adsorption of different cations on the azoic compound, the last peak is red shifted in both experimental and theoretical spectra by about 12, 4, 3 and 3 nm for Azoic/Ni^{2+}, Azoic/Cu^{2+}, Azoic/Zn^{2+} and Azoic/Mg^{2+} respectively in experimental spectra (Fig. 8(a)) and by about 208, 153, 65 and 59 nm for Azoic/Ni^{2+}, Azoic/Cu^{2+}, Azoic/Zn^{2+} and Azoic/Mg^{2+} respectively in theorectical spectra (Fig. 8(b)). The Changes in the position of this band in experimental and theoretical azo benzene-complexe's absorption spectra reffers essentially to metallic electronic structure changes, geometry (valence orbital's spatial arrangements), coordination numbers, effective charge and size, in addition to charge distribution, azoic molecule orbital's suitability to bonding to a metal ion, the ligand steric demands and chelating effect, diffrent metal–azo benzene interaction bond types as well as charge distribution along the metal–azo benzene bond. All these propositions also arise when the coordination object is not a separate metallic ion or numerous combined ions [87]. Moreover, this red shift clearly provides a very interesting index for detecting these cations at sensor devices especially for the detection of Ni^{2+} cation. Besides, we can notice from Table 9 that the most intense peak in the theoretical spectra corresponds to the highest oscillator strength (for example the most intense peak in the theoretical absorption spectra of the isolated molecule Azoic and of the Azoic / Ni^{2+} complex is located at 201 and 429 nm respectively with an important oscillator forces (f) which are 0.313 and 0.503 a. u respectively). Consequently, the oscillator strength is directly related to photon absorption (absorption coefficient) and is inversely proportional to the carrier lifetime. The oscillator strength is given by transition moment integral that relates to the electronic dipole - allowed transition.

Furthermore, the energy gap of HOMO-LUMO is an important value which serves as a stability index. In our case, the energy gap of azoic compound was reduced after the adsorption of Ni^{2+}, Mg^{2+} and Zn^{2+} cations and it was slightly increased after the adsorption of Cu^{2+} cation (Table 7). It implies that the Azoic/Ni^{2+}, Azoic/$Mg^{2+}$and Azoic/Zn^{2+} complexes become more conductive (with lower molecular stability and high reactivity in chemical reactions) compared to isolated azoic molecule, although Azoic/Cu^{2+}complex become more stable compared to isolated azoic compound in the acetonitrile solvent. We can also note that the adsorption of these cations does not change the nature of transition which remains a $\pi \rightarrow \pi^*$ transition. The maximum absorption wavelength corresponds to the electronic transition from the HOMO to LUMO with a contribution of about 50–60% for all complexes.

4.3. Vibrational analysis

As the intensities and the vibrational frequency positions are very sensitive to changes in the molecular structure, the IR spec-

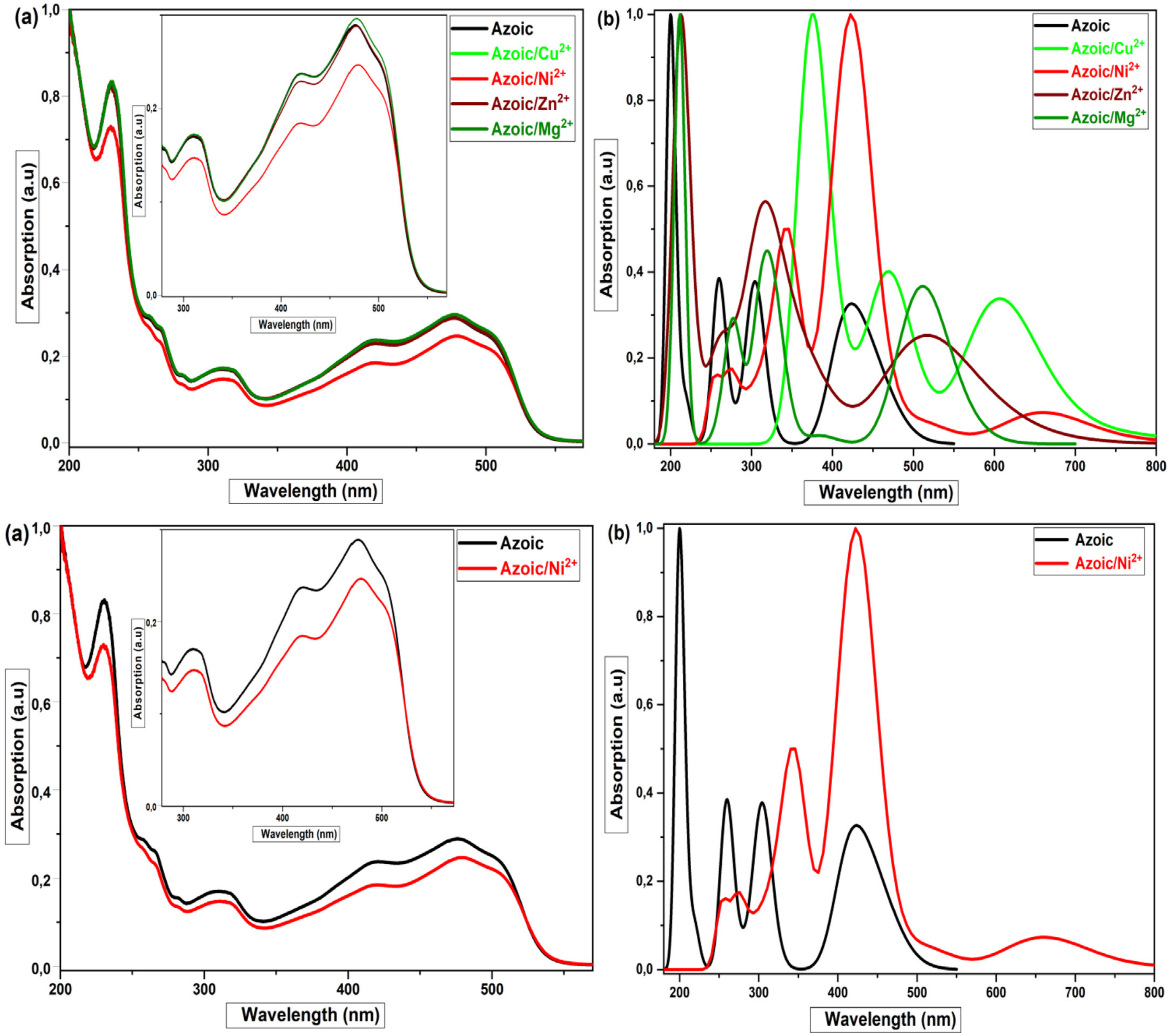

Fig. 8. Calculated absorption spectrum of Azoic compound before and after cations adsorption at 6–311++ *G* (d, p) basis set: **(a)** experimental and **(b)**: theoretical.

Table 9
The experimental and theoretical of the azo molecule before and after the adsorption of the different cations in the acetonitrile solvent.

Isolated Azoic			Azoic/Ni^{2+}			Azoic/Cu^{2+}			Azoic/Zn^{2+}			Azoic/Mg^{2+}		
λ_{Exp} (nm)	λ_{Cal} (nm)	f (a.u)	λ_{Exp} (nm)	λ_{Cal} (nm)	f (a.u)	λ_{Exp} (nm)	λ_{Cal} (nm)	f (a.u)	λ_{Exp} (nm)	λ_{Cal} (nm)	f (a.u)	λ_{Exp} (nm)	λ_{Cal} (nm)	f (a.u)
210	201	0.313	230	272	0.069	230	368	0.052	230	214	0.689	230	213	0.315
234	258	0.299	282	347	0.220	281	378	0.249	265	257	0.106	282	275	0.129
277	307	0.230	318	429	0.503	310	398	0.032	311	316	0.350	311	319	0.257
416	417	0.250	423	511	0.030	421	471	0.135	422	380	0.057	421	385	0.017
476	452	0.157	488	660	0.050	480	605	0.122	479	517	0.240	479	511	0.326

tra can be used to detect the adsorption of Cu^{2+}, Mg^{2+}, Ni^{2+} and Zn^{2+} cations on azoic dye. We present in Fig. 9 the calculated IR spectra before and after adsorption of these cations. One can observe an important difference between the spectra of isolated azoic and azoic/cations. The frequency of (CH oopb+OH oopb+ CC oopb) at 756 cm^{-1} is red-shifted after the adsorption of these cations. The (CH oopb+ CN oopb+ COH twisting) at 832 cm^{-1} is the same before and after cations adsorption but its intensity grows a little from 128 km/mol to 171 km/mol. Upon cations adsorption, the mixed CH ipb+ CC str+ CN str mode of azoic dye at 1206 cm^{-1} is slightly red-shifted by about 6 cm^{-1} (1200 cm^{-1}) while its intensity grows from 15 km/mol to 285, 257, 90 and 25 Km/mol for azoic/Ni^{2+}, azoic/Cu^{2+}, azoic/Zn^{2+} and azoic/Mg^{2+} respectively (Fig. 9(a)). The (CC str+CH *r*+ CO str+ CN str) mode is blue-shifted

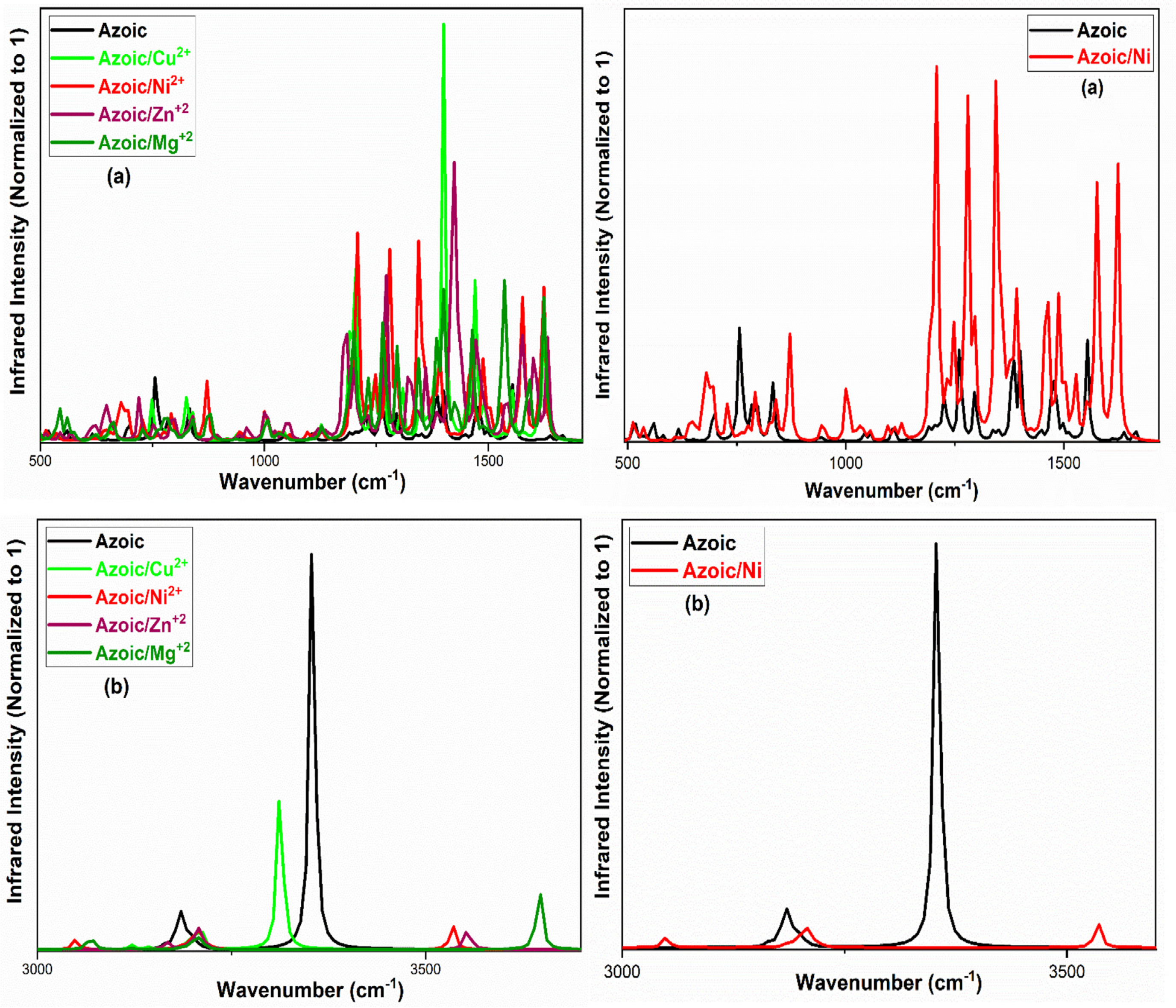

Fig. 9. IR spectra of azobenzene compound before and after Cations adsorption with an enlargement in both area **(a)** and **(b)** using B3LYP-D3/6–311++*G* (d, p) method.

from 1260 cm^{-1} to 1279, 1267,1271 and 1266 cm^{-1} with an intensity enhancement from 88 to 333, 160, 290 and 219 km/mol after the adsorption of Ni^{2+}, Cu^{2+}, Zn^{2+} and Mg^{2+} respectively. The band at 1400 cm^{-1} for azoic dye due to several modes (Table 4) and we notice an increase in intensity after cations adsorption, where the intensity grows from 70 km/mol for isolated azoic dye to 104, 601, 171 and 230 Km/mol for azoic/Ni^{2+}, azoic/Cu^{2+}, azoic/Zn^{2+} and azoic/Mg^{2+} respectively. The band at 1480 cm^{-1} occurs because of several modes in this region of the spectrum. It is slightly blue-shifted (11–8 cm^{-1}) after adsorption of different cations. The band at 1553 cm^{-1}, blue-shifted after adsorption is also due to several active modes. This important change in the IR spectrum constitutes a useful index to detect the binding of cations on azoic dye. The band at 3176–3217 cm^{-1}, red-shifted after the adsorption of all cations. The peak which appears at 3354 cm^{-1}, is blue-shifted after the adsorption of Ni^{2+}, Zn^{2+} and Mg^{2+} by about 180, 200 and 292 cm^{-1} respectively, while it is red-shifted after the adsorption of Cu^{2+} by about 42 cm^{-1} (Fig. 9(b)). The intensities of these bands decrease in a remarkable way after the adsorption of these cations, where they pass from 26 Km/mol for isolated azoic dye to 37, 259, 35 and 99 Km/mol for azoic/Ni^{2+}, azoic/Cu^{2+}, azoic/Zn^{2+} and azoic/Mg^{2+}. The infrared spectra of azoic dye and their complexes with different cations, clearly show a significant effect on the vibrational spectra after adsorption of these cations for all complexes studied here. These frequencies' change of frequency can be related to the interaction between the title cations and the hydrogen bonding zone.

5. Conclusion

In summary, we have described the synthesis of I-phenyl azo-2-naphthol and we have studied the optoelectronic properties of the mentioned compound experimentally and theoretically in different solvents. The MEP, NPA and NBO were computed using B3LYP-D3/6–311++*G* (d, p) method to understand the atomic charge distribution of the azoic dye and to identify the way in which the molecules interact with each other. The most stable geometry was characterized for the azobenzene in Acetonitrile. The vibrational frequencies of the fundamental modes of this molecule have been accurately assigned and investigated in gas phase. The absorption spectra were carried out by TD-DFT method in gas and other solvents and compared with the experimental one. In order to assess the potential role of the synthesized azoic dye as a cation's sensor, structures were also characterized for Cu^{2+}, Mg^{2+}, Ni^{2+} and Zn^{2+} adsorbed complexes. A clear sigma bonding chemisorption of cations on N$_{19}$ atom is observed for all complexes, followed by a charge transfer from the cations (Cu^{2+}, Mg^{2+}, Ni^{2+} and Zn^{2+}) to the strong hydrogen bonding zone. Adsorption energies were performed, in both gas and acetonitrile solvent, to understand the nature of the involved interactions between I-phenyl azo-2-naphthol and different cations. Results indicate that the azoic/Ni^{2+} is the most favorable complex in both gas and liquid phase, where the adsorption energy is found to be -330.374 kcal/mol and -119.743 kcal/mol respectively. Furthermore, after cations chemisorption on azoic compound, a remarkable red shift is observed in the optical spectra, especially with azoic/Ni^{2+} complex, offering thus a very good index to detect the binding of Ni^{2+}. The IR spectra analysis also shows a significant change in the signal strengths and vibrational frequencies. The optical spectra, energy gap and the vibrational spectra can therefore be used to detect the presence of different cations and azoic dye show appropriate properties to constitute good Ni^{2+} sensors.

Declaration of Competing Interest

The authors declare that they have no conflict of interest.

CRediT authorship contribution statement

Marwa Chaabene: Data curation, Software, Writing - original draft. **Soumaya Agren:** Investigation, Software, Writing - original draft. **Jamal El Haskouri:** Data curation, Software. **Abdul-Rahman Allouche:** Formal analysis, Resources. **Lahcini Mohamed:** Funding acquisition, Validation. **Rafik Ben Chaâbane:** Methodology, Validation. **Mohamed Hassen V Baouab:** Project administration, Methodology.

Acknowledgements

The authors greatly acknowledge financial support between cooperation Tunisia-Morocco for funding the work through the research group N° **17/TM10**.

References

[1] M. Zhang, Y.-Q. Liu, B.-C. Ye, Colorimetric assay for parallel detection of Cd^{2+}, Ni^{2+} and Co^{2+} using peptide-modified gold nanoparticles, Analyst 137 (2012) 601–607, doi:10.1039/C1AN15909G.

[2] P.D. Zalewski, S.H. Millard, I.J. Forbes, O. Kapaniris, A. Slavotinek, W.H. Betts, A.D. Ward, S.F. Lincoln, I. Mahadevan, Video image analysis of labile zinc in viable pancreatic islet cells using a specific fluorescent probe for zinc, J. Histochem. Cytochem. 42 (1994) 877–884, doi:10.1177/42.7.8014471.

[3] P. As, Discovery and importance of zinc in human nutrition, Fed. Proc. 43 (1984) 2829–2834.

[4] B. Shao, L. Mao, N. Qu, Y.-F. Wang, H.-Y. Gao, F. Li, L. Qin, J. Shao, C.-H. Huang, D. Xu, L.-N. Xie, C. Shen, X. Zhou, B.-Z. Zhu, Mechanism of synergistic DNA damage induced by the hydroquinone metabolite of brominated phenolic environmental pollutants and Cu(II): formation of DNA-Cu complex and site-specific production of hydroxyl radicals, Free Radic. Biol. Med. 104 (2017) 54–63, doi:10.1016/j.freeradbiomed.2016.12.050.

[5] V. Kumar, J. Kalita, H.K. Bora, U.K. Misra, Temporal kinetics of organ damage in copper toxicity: a histopathological correlation in rat model, Regul. Toxicol. Pharmacol. 81 (2016) 372–380, doi:10.1016/j.yrtph.2016.09.025.

[6] M.G. Morales, Y. Vazquez, M.J. Acuña, J.C. Rivera, F. Simon, J.D. Salas, J. Álvarez Ruf, E. Brandan, C. Cabello-Verrugio, Angiotensin II-induced pro-fibrotic effects require p38MAPK activity and transforming growth factor beta 1 expression in skeletal muscle cells, Int. J. Biochem. Cell Biol. 44 (2012) 1993–2002, doi:10.1016/j.biocel.2012.07.028.

[7] J. Jiang, W. Liu, J. Cheng, L. Yang, H. Jiang, D. Bai, W. Liu, A sensitive colorimetric and ratiometric fluorescent probe for mercury species in aqueous solution and living cells, Chem. Commun. 48 (2012) 8371–8373, doi:10.1039/C2CC32867D.

[8] M. Hosseini, A. Ghafarloo, M.R. Ganjali, F. Faridbod, P. Norouzi, M.S. Niasari, A turn-on fluorescent sensor for Zn2+ based on new Schiff's base derivative in aqueous media, Sens. Actuators B 198 (2014) 411–415, doi:10.1016/j.snb.2014.03.061.

[9] K.S. Kasprzak, B.A. Diwan, J.M. Rice, M. Misra, C.W. Riggs, R. Olinski, M. Dizdaroglu, Nickel(II)-mediated oxidative DNA base damage in renal and hepatic chromatin of pregnant rats and their fetuses. Possible relevance to carcinogenesis, Chem. Res. Toxicol. 5 (1992) 809–815, doi:10.1021/tx00030a013.

[10] J. Zhou, B. Du, Z. Wang, W. Zhang, L. Xu, X. Fan, X. Liu, J. Zhou, Distributions and pools of lead (Pb) in a terrestrial forest ecosystem with highly elevated atmospheric Pb deposition and ecological risks to insects, Sci. Total Environ. 647 (2019) 932–941, doi:10.1016/j.scitotenv.2018.08.091.

[11] A. Ricolleau, N. Floquet, J.-L. Devidal, R.J. Bodnar, J. Perrin, J. Garrabou, J.-.G. Harmelin, F. Costantini, J.R. Boavida, D. Vielzeuf, Lead (Pb) profiles in red coral skeletons as high resolution records of pollution in the Mediterranean Sea, Chem. Geol. 525 (2019) 112–124, doi:10.1016/j.chemgeo.2019.07.005.

[12] A.J. Specht, Y. Lin, M. Weisskopf, C. Yan, H. Hu, J. Xu, L.H. Nie, XRF-measured bone lead (Pb) as a biomarker for Pb exposure and toxicity among children diagnosed with Pb poisoning, Biomarkers 21 (2016) 347–352, doi:10.3109/1354750X.2016.1139183.

[13] A Delicious Bone-Building Burrito, Each Ingredient Is A Rich Source Of Magnesium Or Manganese, Save Our Bones, 2017 https://saveourbones.com/a-delicious-bone-building-burrito-each-ingredient-is-a-rich-source-of-magnesium-or-manganese/(accessed July 17, 2020.

[14] A.A. Mozeto, W. de, F. Jardim, A Química Ambiental no Brasil, Química Nova 25 (2002) 7–11, doi:10.1590/S0100-40422002000800002.

[15] J. Pei, X. Yu, Z. Zhang, J. Zhang, S. Wei, R. Boukherroub, In-situ graphene modified self-supported boron-doped diamond electrode for Pb(II) electrochemical detection in seawater, Appl. Surf. Sci. 527 (2020) 146761, doi:10.1016/j.apsusc.2020.146761.

[16] J. Zhang, Y. Liu, Q. Fei, H. Shan, F. Chen, Q. Liu, G. Chai, G. Feng, Y. Huan, A salicylal-derived Schiff base as Co (II) selective fluorescent probe, Sens. Actuators B 239 (2017) 203–210, doi:10.1016/j.snb.2016.07.178.

[17] Y.-F. Sun, J.-J. Li, F. Xie, Y. Wei, M. Yang, Ruthenium-loaded cerium dioxide nanocomposites with rich oxygen vacancies promoted the highly sensitive electrochemical detection of Hg(II), Sens. Actuators B 320 (2020) 128355, doi:10.1016/j.snb.2020.128355.

[18] B. Majidi, A. Amiri, A. Badiei, A. Shayesteh, Dual mode colorimetric-fluorescent sensor for highly sensitive and selective detection of Mg2+ ion in aqueous media, J. Mol. Struct. 1213 (2020) 128156, doi:10.1016/j.molstruc.2020.128156.

[19] Z. Ghasemi, A. Mohammadi, Sensitive and selective colorimetric detection of Cu (II) in water samples by thiazolylazopyrimidine-functionalized TiO2 nanoparticles, Spectrochim. Acta Part A 239 (2020) 118554, doi:10.1016/j.saa.2020.118554.

[20] Q. Liu, J. Li, W. Yang, X. Zhang, C. Zhang, C. Labbé, X. Portier, F. Liu, J. Yao, B. Liu, Simultaneous detection of trace Ag(I) and Cu(II) ions using homoepitaxially grown GaN micropillar electrode, Anal. Chim. Acta 1100 (2020) 22–30, doi:10.1016/j.aca.2019.11.010.

[21] N.R. Chereddy, P. Nagaraju, M.V. Niladri Raju, V.R. Krishnaswamy, P.S. Korrapati, P.R. Bangal, V.J. Rao, A novel FRET 'off–on' fluorescent probe for the selective detection of Fe3+, Al3+ and Cr3+ ions: its ultrafast energy transfer kinetics and application in live cell imaging, Biosens. Bioelectron. 68 (2015) 749–756, doi:10.1016/j.bios.2015.01.074.

[22] S. Benkhaya, S. M'rabet, A. El Harfi, Classifications, properties, Recent Synthesis and Applications of Azo dyes, Heliyon. 6 (2020) e03271. https://doi.org/10.1016/j.heliyon.2020.e03271.

[23] Ö. Arslan, B. Aydıner, E. Yalçın, B. Babür, N. Seferoğlu, Z. Seferoğlu, 8-Hydroxyquinoline based push-pull azo dye: novel colorimetric chemosensor for anion detection, J. Mol. Struct. 1149 (2017) 499–509, doi:10.1016/j.molstruc.2017.08.001.

[24] M. Ali, A. Mansha, S. Asim, M. Zahid, M. Usman, N. Ali, DFT Study for the Spectroscopic and Structural Analysis of p-Dimethylaminoazobenzene, Journal of Spectroscopy 2018 (2018) 1–15, doi:10.1155/2018/9365153.

[25] M.C. Sreenath, S. Mathew, I.Hubert Joe, V.K. Rastogi, Z-scan measurements of the third-order optical nonlinearities and vibrational spectral studies by DFT computations on azo dye 1-(2-Methylphenylazo)-2-napthol, Opt. Laser Technol. 97 (2017) 390–399, doi:10.1016/j.optlastec.2017.07.032.

[26] W. Huang, Z. Chen, H. Lin, H. Lin, A novel thiourea–hydrazone-based switch-on fluorescent chemosensor for acetate, J. Lumin. 131 (2011) 592–596, doi:10.1016/j.jlumin.2010.10.036.

[27] Y. Zhou, J.F. Zhang, J. Yoon, Fluorescence and Colorimetric Chemosensors for Fluoride-Ion Detection, Chem. Rev. 114 (2014) 5511–5571, doi:10.1021/cr400352m.

[28] R. Joseph, B. Ramanujam, A. Acharya, C.P. Rao, Fluorescence switch-on sensor for Cu2+ by an amide linked lower rim 1,3-bis(2-picolyl)amine derivative of calix[4]arene in aqueous methanol, Tetrahedron Lett. 50 (2009) 2735–2739, doi:10.1016/j.tetlet.2009.03.109.

[29] R. Joseph, B. Ramanujam, A. Acharya, A. Khutia, C.P. Rao, Experimental and Computational Studies of Selective Recognition of Hg2+ by Amide Linked Lower Rim 1,3-Dibenzimidazole Derivative of Calix[4]arene: species Characterization in Solution and that in the Isolated Complex, Including the Delineation of the Nanostructures, J. Org. Chem. 73 (2008) 5745–5758, doi:10.1021/jo800073g.

[30] R. Joseph, B. Ramanujam, H. Pal, C.P. Rao, Lower rim 1,3-di-amide-derivative of calix[4]arene possessing bis-{N-(2,2′-dipyridylamide)} pendants: a dual flu-

orescence sensor for Zn2+ and Ni2+, Tetrahedron Lett. 49 (2008) 6257–6261, doi:10.1016/j.tetlet.2008.08.049.

[31] J. Dessingou, R. Joseph, C.P. Rao, A direct fluorescence-on chemo-sensor for selective recognition of Zn(II) by a lower rim 1,3-di-derivative of calix[4]arene possessing bis-{N-(2-hydroxynaphthyl-1-methylimine)} pendants, Tetrahedron Lett. 46 (2005) 7967–7971, doi:10.1016/j.tetlet.2005.09.079.

[32] R.K. Pathak, Sk.Md. Ibrahim, C.P. Rao, Selective recognition of Zn2+ by salicylaldimine appended triazole-linked di-derivatives of calix[4]arene by enhanced fluorescence emission in aqueous-organic solutions: role of terminal –CH2OH moietieefs in conjunction with the imine in recognition, Tetrahedron Lett. 50 (2009) 2730–2734, doi:10.1016/j.tetlet.2009.03.126.

[33] K. Choi, A.D. Hamilton, Selective Anion Binding by a Macrocycle with Convergent Hydrogen Bonding Functionality, J. Am. Chem. Soc. 123 (2001) 2456–2457, doi:10.1021/ja005772+.

[34] M.J. Frisch, G.W. Trucks, H.B. Schlegel, G.E. Scuseria, Gaussian 09, Revision A.02 M. A. Robb, J. R. Cheeseman, G. Scalmani, V. Barone, G. A. Petersson, H. Nakatsuji, X. Li, M. Caricato, A. Marenich, J. Bloino, B. G. Janesko, R. Gomperts, B. Mennucci, H. P. Hratchian, J. V. Ortiz, A. F. Izmaylov, J. L. Sonnenberg, D. Williams-Young, F. Ding, F. Lipparini, F. Egidi, J. Goings, B. Peng, A. Petrone, T. Henderson, D. Ranasinghe, V. G. Zakrzewski, J. Gao, N. Rega, G. Zheng, W. Liang, M. Hada, M. Ehara, K. Toyota, R. Fukuda, J. Hasegawa, M. Ishida, T. Nakajima, Y. Honda, O. Kitao, H. Nakai, T. Vreven, K. Throssell, J. A. Montgomery, Jr., J. E. Peralta, F. Ogliaro, M. Bearpark, J. J. Heyd, E. Brothers, K. N. Kudin, V. N. Staroverov, T. Keith, R. Kobayashi, J. Normand, K. Raghavachari, A. Rendell, J. C. Burant, S. S. Iyengar, J. Tomasi, M. Cossi, J. M. Millam, M. Klene, C. Adamo, R. Cammi, J. W. Ochterski, R. L. Martin, K. Morokuma, O. Farkas, J. B. Foresman, and D. J. Fox, Gaussian, Inc., Wallingford CT, 2016.

[35] Gabedit—A graphical user interface for computational chemistry softwares - Allouche - A.-R, J. Comput. Chem. 32 (2011) 174–182.

[36] R.-I. Dennington, T. Keith, J. Millam, GaussView, Version 5.0.8, Semichem. Inc., Shawnee Mission, KS, 2008.

[37] S. Grimme, J. Antony, S. Ehrlich, H. Krieg, A consistent and accurate ab initio parametrization of density functional dispersion correction (DFT-D) for the 94 elements H-Pu, J. Chem. Phys. 132 (2010) 154104, doi:10.1063/1.3382344.

[38] K. Wolinski, J.F. Hinton, P. Pulay, Efficient implementation of the gauge-independent atomic orbital method for NMR chemical shift calculations, J. Am. Chem. Soc. 112 (1990) 8251–8260, doi:10.1021/ja00179a005.

[39] D. Sarkar, A.K. Pramanik, T.K. Mondal, Benzimidazole based ratiometric and colourimetric chemosensor for Ni(II), Spectrochim. Acta Part A 153 (2016) 397–401, doi:10.1016/j.saa.2015.08.052.

[40] S.F. Boys, F. Bernardi, The calculation of small molecular interactions by the differences of separate total energies. Some procedures with reduced errors, Mol. Phys. 19 (1970) 553–566, doi:10.1080/00268977000101561.

[41] G. Attia, S. Rahali, S. Teka, N. Fourati, C. Zerrouki, M. Seydou, S. Chehimi, S. Hayouni, J.-P. Mbakidi, S. Bouquillon, M. Majdoub, R.B. Chaabane, Anthracene based surface acoustic wave sensors for picomolar detection of lead ions. Correlation between experimental results and DFT calculations, Sens. Actuators B 276 (2018) 349–355, doi:10.1016/j.snb.2018.08.033.

[42] A.S. Rad, N. Nasimi, M. Jafari, D.S. Shabestari, E. Gerami, Ab-initio study of interaction of some atmospheric gases (SO2, NH3, H2O, CO, CH4 and CO2) with polypyrrole (3PPy) gas sensor: DFT calculations, Sensors and Actuators B: Chemical. C (2015) 641–651, doi:10.1016/j.snb.2015.06.019.

[43] N.N. Matsuzawa, A. Ishitani, D.A. Dixon, T. Uda, Time-Dependent Density Functional Theory Calculations of Photoabsorption Spectra in the Vacuum Ultraviolet Region, J. Phys. Chem. A. 105 (2001) 4953–4962, doi:10.1021/jp003937v.

[44] J.-L. Calais, Density-functional Theory of Atoms and Molecules, Oxford University Press, New York, Oxford, 1989 R.G. Parr and W. YangIX + 333 pp. Price £45.00, International Journal of Quantum Chemistry. 47 (1993) 101–101, doi:10.1002/qua.560470107.

[45] M.R. Zamanloo, A. nasser Shamkhali, M. Alizadeh, Y. Mansoori, G. Imanzadeh, A novel barbituric acid-based azo dye and its derived polyamides: synthesis, spectroscopic investigation and computational calculations, Dyes Pigm. 95 (2012) 587–599, doi:10.1016/j.dyepig.2012.05.028.

[46] M. Cinar, A. Coruh, M. Karabacak, UV–vis FT-IR, 1H and 13C NMR spectra and the equilibrium structure of organic dye molecule disperse red 1 acrylate: a combined experimental and theoretical analysis, Spectrochim. Acta Part A 83 (2011) 561–569, doi:10.1016/j.saa.2011.09.003.

[47] J.-E. Lee, H.J. Kim, M.R. Han, S.Y. Lee, W.J. Jo, S.S. Lee, J.S. Lee, Crystal structures of C.I. Disperse Red 65 and C.I. Disperse Red 73, Dyes Pigm. 80 (2009) 181–186, doi:10.1016/j.dyepig.2008.07.001.

[48] O. Noureddine, S. Gatfaoui, S.A. Brandan, A. Sagaama, H. Marouani, N. Issaoui, Experimental and DFT studies on the molecular structure, spectroscopic properties, and molecular docking of 4-phenylpiperazine-1-ium dihydrogen phosphate, J. Mol. Struct. 1207 (2020) 127762, doi:10.1016/j.molstruc.2020.127762.

[49] T.Ben Issa, A. Sagaama, N. Issaoui, Computational study of 3-thiophene acetic acid: molecular docking, electronic and intermolecular interactions investigations, Comput. Biol. Chem. 86 (2020) 107268, doi:10.1016/j.compbiolchem.2020.107268.

[50] F.J. Luque, J.M. López, M. Orozco, Perspective on “Electrostatic interactions of a solute with a continuum. A direct utilization of ab initio molecular potentials for the prevision of solvent effects, Theor. Chem. Acc. 103 (2000) 343–345, doi:10.1007/s002149900013.

[51] E. Scrocco, J. Tomasi, The electrostatic molecular potential as a tool for the interpretation of molecular properties, in: New Concepts II, Springer, Berlin, Heidelberg, 1973, pp. 95–170, doi:10.1007/3-540-06399-4_6.

[52] P. Politzer, M.C. Concha, J.S. Murray, Density functional study of dimers of dimethylnitramine, Int. J. Quantum Chem. 80 (2000) 184–192 https://doi.org/10.1002/1097-461X(2000)80:2<184::AID−QUA12>3.0.CO;2-O.

[53] M. Chaabene, S. Agren, A.-R. Allouche, M. Lahcinie, R.B. Chaâbane, M.H.V. Baouab, Theoretical and experimental investigations of complexation with BF$_3$.Et$_2$O effects on electronic structures, energies and photophysical properties of Anil and tetraphenyl (hydroxyl) imidazol, Appl. Organomet. Chem. 33 (2019) e5218, doi:10.1002/aoc.5218.

[54] M. Erfantalab, H. Khanmohammadi, New 1, 2, 4-triazole-based azo–azomethine dye. Part III: synthesis, characterization, thermal property, spectrophotometric and computational studies, Spectrochim. Acta Part A 125 (2014) 345–352, doi:10.1016/j.saa.2014.01.113.

[55] M. Cinar, A. Coruh, M. Karabacak, A comparative study of selected disperse azo dye derivatives based on spectroscopic (FT-IR, NMR and UV–Vis) and nonlinear optical behaviors, Spectrochim. Acta Part A 122 (2014) 682–689, doi:10.1016/j.saa.2013.11.106.

[56] S. Agren, M. Chaabene, A. Allouche, R. Ben Chaâbane, M. Lahcinie, M.H.V. Baouab, Blue Highly Fluorescent Boranil Derived From Anil Ligand: synthesis, Characterization, Experimental and Theoretical Evaluation of Solvent Effect on Structures and Photophysical Properties, Appl. Organomet. Chem. (2020), doi:10.1002/aoc.5764.

[57] NIST Computational Chemistry Comparison and Benchmark Database, NIST Standard Reference Database Number 101, 2018 Release 19, AprilEditor: Russell D. Johnson III, http://cccbdb.nist.gov/.

[58] M.K. Subramanian, P.M. Anbarasan, V. Ilangovan, N. Sundaraganesan, FT-IR, FT-Raman spectra and DFT vibrational analysis of 2-aminobiphenyl, Mol. Simul. 34 (2008) 277–287, doi:10.1080/08927020701829856.

[59] N. Sundaraganesan, S. Illakiamani, C. Meganathan, B.D. Joshua, Vibrational spectroscopy investigation using ab initio and density functional theory analysis on the structure of 3-aminobenzotrifluoride, Spectrochim. Acta Part A 67 (2007) 214–224, doi:10.1016/j.saa.2006.07.004.

[60] K. Chandrasekaran, R. Thilak Kumar, Structural, spectral, thermodynamical, NLO, HOMO, LUMO and NBO analysis of fluconazole, Spectrochim. Acta Part A 150 (2015) 974–991, doi:10.1016/j.saa.2015.06.018.

[61] A. Teimouri, A.N. Chermahini, K. Taban, H.A. Dabbagh, Experimental and CIS, TD-DFT, ab initio calculations of visible spectra and the vibrational frequencies of sulfonyl azide-azoic dyes, Spectrochim. Acta Part A 72 (2009) 369–377, doi:10.1016/j.saa.2008.10.006.

[62] K.B. Benzon, H.T. Varghese, C.Y. Panicker, K. Pradhan, B.K. Tiwary, A.K. Nanda, C.V. Alsenoy, Spectroscopic investigation (FT-IR and FT-Raman), vibrational assignments, HOMO–LUMO, NBO, MEP analysis and molecular docking study of 2-(4-hydroxyphenyl)-4,5-dimethyl-1H-imidazole 3-oxide, Spectrochim. Acta Part A 146 (2015) 307–322, doi:10.1016/j.saa.2015.03.063.

[63] V. Krishnakumar, M. Arivazhagan, Vibrational and normal coordinate analysis of xanthine and hypoxanthine, IJPAP 42 (06) (2004) [June 2004] http://nopr.niscair.res.in/handle/123456789/26125 . (accessed June 1, 2020.

[64] K. Chandrasekaran, R. Thilak Kumar, Structural, spectral, thermodynamical, NLO, HOMO, LUMO and NBO analysis of fluconazole, Spectrochim. Acta Part A 150 (2015) 974–991, doi:10.1016/j.saa.2015.06.018.

[65] K. Kumanan, R.R. Muhamed, M. Raja, V. Sathyanarayanamoorthi, M.Y. Mowlana, S. Arulappan, Molecular docking, Spectroscopic, NLO, NBO and antimicrobial analysis of (Z)-3-(3-bromophenyl)-1-(1H-imidazol-1-yl) prop-2-en-1-one, International Journal of Advanced Research and Development 2 (2017) 568–576.

[66] D. Michalska, D.C. Bieńko, A.J. Abkowicz-Bieńko, Z. Latajka, Density Functional, Hartree−Fock, and MP2 Studies on the Vibrational Spectrum of Phenol, J. Phys. Chem. 100 (1996) 17786–17790, doi:10.1021/jp961376v.

[67] K.S.B. Ram, Vibrational Spectroscopic Analysis with Chemical Computations for NLO Molecule Benzilic Acid 6 (2018) 7.

[68] N. Sundaraganesan, H. Saleem, S. Mohan, Vibrational spectra, assignments and normal coordinate analysis of 3-aminobenzyl alcohol, Spectrochim. Acta Part A 59 (2003) 2511–2517, doi:10.1016/S1386-1425(03)00037-4.

[69] N. Sundaraganesan, C. Meganathan, B.D. Joshua, P. Mani, A. Jayaprakash, Molecular structure and vibrational spectra of 3-chloro-4-fluoro benzonitrile by ab initio HF and density functional method, Spectrochim. Acta Part A 71 (2008) 1134–1139, doi:10.1016/j.saa.2008.03.019.

[70] I.D. Sadekov, V.I. Minkin, A.E. Lutskii, The Intramolecular Hydrogen Bond and the Reactivity of Organic Compounds, Russ. Chem. Rev. 39 (1970) 179, doi:10.1070/RC1970v039n03ABEH001950.

[71] H. Tanak, K. Pawlus, M.K. Marchewka, Molecular structure, vibrational spectra and DFT computational studies of melaminium N-acetylglycinate dihydrate, J. Mol. Struct. 1121 (2016) 142–155, doi:10.1016/j.molstruc.2016.05.059.

[72] M.R. Maliyappa, J. Keshavayya, N.M. Mallikarjuna, P. Murali Krishna, N. Shivakumara, T. Sandeep, K. Sailaja, M.A. Nazrulla, Synthesis, characterization, pharmacological and computational studies of 4, 5, 6, 7-tetrahydro-1, 3-benzothiazole incorporated azo dyes, J. Mol. Struct. 1179 (2019) 630–641, doi:10.1016/j.molstruc.2018.11.041.

[73] M. Karabacak, A. Çoruh, M. Kurt, FT-Raman FT-IR, NMR spectra, and molecular structure investigation of 2,3-dibromo-N-methylmaleimide: a combined experimental and theoretical study, J. Mol. Struct. 892 (2008) 125–131, doi:10.1016/j.molstruc.2008.05.014.

[74] M.C. Sreenath, I.H. Joe, V.K. Rastogi, Experimental and theoretical investigation of third-order nonlinear optical properties of azo dye 1-(2, 5-Dimethoxy-phenylazo)-naphthalen-2-ol by Z-scan technique and quantum chemical computations, Dyes Pigm. 157 (2018) 163–178.

[75] Y. Yu, G. Li, J. Liu, D. Yuan, A recyclable fluorescent covalent organic framework for exclusive detection and removal of mercury(II), Chem. Eng. J. 401 (2020) 126139, doi:10.1016/j.cej.2020.126139.

[76] P.T. Tasli, Ç.K. Atay, T. Demirturk, T. Tilki, Experimental and computational studies of newly synthesized azo dyes based materials, J. Mol. Struct. 1201 (2020) 127098, doi:10.1016/j.molstruc.2019.127098.

[77] A. Mohammadi, B. Khalili, M. Tahavor, Novel push–pull heterocyclic azo disperse dyes containing piperazine moiety: synthesis, spectral properties, antioxidant activity and dyeing performance on polyester fibers, Spectrochim. Acta Part A 150 (2015) 799–805, doi:10.1016/j.saa.2015.06.024.

[78] R.L. Reeves, M.S. Maggio, L.F. Costa, Importance of solvent cohesion and structure in solvent effects on binding site probes, J. Am. Chem. Soc. 96 (1974) 5917–5925, doi:10.1021/ja00825a032.

[79] M. Urban, K. Durka, P. Jankowski, J. Serwatowski, S. Luliński, Highly Fluorescent Red-Light Emitting Bis(boranils) Based on Naphthalene Backbone, J. Org. Chem. 82 (2017) 8234–8241, doi:10.1021/acs.joc.7b01001.

[80] H. Zhang, C. Liu, Synthesis and properties of furan/thiophene substituted difluoroboron β-diketonate derivatives bearing a triphenylamine moiety, Dyes Pigm. 143 (2017) 143–150, doi:10.1016/j.dyepig.2017.04.022.

[81] J. Griffiths, K.-.C. Feng, The influence of intramolecular hydrogen bonding on the order parameter and photostability properties of dichroic azo dyes in a nematic liquid crystal host, J. Mater. Chem. 9 (1999) 2333–2338, doi:10.1039/A901936G.

[82] R. Gup, E. Giziroglu, B. Kırkan, Synthesis and spectroscopic properties of new azo-dyes and azo-metal complexes derived from barbituric acid and aminoquinoline, Dyes Pigm. 73 (2007) 40–46, doi:10.1016/j.dyepig.2005.10.005.

[83] F.S. Freyria, B. Bonelli, R. Sethi, M. Armandi, E. Belluso, E. Garrone, Reactions of Acid Orange 7 with Iron Nanoparticles in Aqueous Solutions, J. Phys. Chem. C. 115 (2011) 24143–24152, doi:10.1021/jp204762u.

[84] B. Mandal, A. Mondal, Solar light sensitive samarium-doped ceria photocatalysts: microwave synthesis, characterization and photodegradation of Acid Orange 7 at atmospheric conditions and in the absence of any oxidizing agents, RSC Adv. 5 (2015) 43081–43091, doi:10.1039/C5RA03758A.

[85] M. Chaabene, B. Gassoumi, P. Mignon, R. Ben Chaâbane, A.-.R. Allouche, New zinc phthalocyanine derivatives for nitrogen dioxide sensors: a theoretical optoelectronic investigation, J. Mol. Graph. Model. 88 (2019) 174–182, doi:10.1016/j.jmgm.2019.01.008.

[86] R. Soury, M. Chaabene, M. Jabli, T.A. Saleh, R. Ben Chaabane, E. Saint-Aman, F. Loiseau, C. Philouze, A.-.R. Allouche, H. Nasri, Meso-tetrakis(3,4,5-trimethoxyphenyl)porphyrin derivatives: synthesis, spectroscopic characterizations and adsorption of NO2, Chem. Eng. J. 375 (2019) 122005, doi:10.1016/j.cej.2019.122005.

[87] M. Gaber, Y.S. El-Sayed, K. El-Baradie, R.M. Fahmy, Cu(II) complexes of monobasic bi- or tridentate (NO, NNO) azo dye ligands: synthesis, characterization, and interaction with Cu-nanoparticles, J. Mol. Struct. 1032 (2013) 185–194, doi:10.1016/j.molstruc.2012.07.019.